Neuroanatomical and behavioral characterization of corticotropin releasing factor-expressing lateral Habenula neurons in mice

William J. Flerlage[1,#], Shawn C. Gouty[1, #], Emily H. Thomas[1, #], Sarah C. Simmons[1], Mumeko C. Tsuda[2], Oana L. Rujan[1], Regina C. Armstrong[4], Catherine M. Davis[1], Laxmi Iyer[3], Emily Petrus[4], Brian M. Cox[1], T. John Wu[5], Fereshteh S. Nugent[1].

[1]Uniformed Services University of the Health Sciences, Department of Pharmacology and Molecular Therapeutics, Bethesda, MD 20814, USA.

[2] Uniformed Services University of the Health Sciences, Preclinical Behavior and Modeling Core, Bethesda, MD 20814, USA.

[3]Henry M. Jackson Foundation for the Advancement of Military Medicine, Bethesda MD 20817

[4]Uniformed Services University of the Health Sciences, Department of Anatomy, Physiology, and Genetics, Bethesda, MD 20814, USA.

[5] Uniformed Services University of the Health Sciences, Department of Gynecologic Surgery and Obstetrics, Bethesda, MD 20814, USA.

[#] These authors contributed equally

* To whom correspondence should be addressed:

Fereshteh S. Nugent, Ph.D., Edward Hebert School of Medicine, Department of Pharmacology, Uniformed Services University of the Health Sciences, 4301 Jones Bridge Road, Bethesda, Maryland 20814, fereshteh.nugent@usuhs.edu

Abstract

The lateral habenula (LHb) is a critical hub for stress-related behaviors, yet the sources of its corticotropin-releasing factor (CRF) inputs remain poorly defined. Using high-resolution imaging, RNAscope, and viral tracing, we identified a novel, intrinsic population of CRF-expressing LHb neurons (LHb^{CRF}). These neurons are primarily VGLUT2+, though a rostral subpopulation co-expresses GAD2. While chemogenetic activation of LHb^{CRF} neurons did not impact place preference or anxiety-like behaviors, it selectively biased defensive strategies toward passive action-locking during the Visual Looming Shadow Test (VLST). Notably, this activation prolonged escape latencies in males and post-escape shelter stays in females. Electrophysiological and optogenetic characterization revealed significant sexual dimorphism: male LHb^{CRF} neurons are more numerous and intrinsically excitable, whereas female LHb^{CRF} neurons exhibit stronger local excitatory connectivity. These findings establish LHb^{CRF} neurons as a sexually dimorphic circuit component that could modulate sex-specific defensive strategies under threat via divergent cellular and synaptic mechanisms between the sexes.

Introduction

The lateral habenula (LHb) is an evolutionarily conserved brain region crucial for behavioral selection, in response to stressors and rewards; thereby guiding goal-directed motivated behavior[1-3]. Ongoing research continues to unveil nuanced roles for the LHb in both normal behavior and the pathophysiology of mental illness. Aversive stimuli as well as the omission of expected reward generally activate the LHb, and its hyperactivity is implicated in anhedonic and negative states associated with depression, anxiety, and drug addiction. Conversely, reward-related stimuli inhibit LHb activity which generates positive motivational states. These findings highlight LHb's therapeutic potential, as evidenced by the anti-depressant effects of deep brain stimulation of the LHb and ketamine's NMDA receptor antagonism of LHb neurons [1-5].

The majority of LHb neurons are glutamatergic, and express markers such as the vesicular glutamate transporter 2 (VGLUT2) [6]. However, a small subset also expresses classical GABAergic markers, including glutamic acid decarboxylase 1 (GAD1), GAD2, the GABA transporter 1 (GAT-1), and the vesicular GABA transporter (VGAT), suggesting the presence of a functional intrinsic inhibitory circuit within the LHb[7-11]. Notably, some LHb neurons co-express both glutamatergic and GABAergic markers. For example, parvalbumin-expressing LHb neurons (LHb^{PV}) comprise three distinct subpopulations: a majority that are VGLUT2+ and glutamatergic, a subset that expresses only GABAergic markers, and a subpopulation that co-expresses both glutamatergic and GABAergic markers (e.g., VGLUT2 and GAD2)[7]. Most LHb glutamatergic outputs directly and indirectly modulate key monoaminergic systems, primarily the dopamine and serotonin pathways that encode behavioral avoidance and

reward prediction errors. Mechanistically, this involves suppressing dopamine release from the ventral tegmental area (VTA) and serotonin release from the raphe nuclei by exciting GABAergic neurons, particularly those in the rostromedial tegmental area (RMTg), thus shifting behavior away from reward-seeking[2,12-14]. Consequently, LHb is increasingly recognized as a critical structure in the neural circuits that govern mood, motivation, and decision-making by processing a diverse array of appetitive and aversive signals that are crucial for adaptive behavior, allowing organisms to learn from both positive and negative experiences[5].

LHb neuronal activity is regulated by glutamatergic, GABAergic, and glutamate/GABA co-releasing synaptic inputs from various regions in the forebrain and midbrain such as the medial prefrontal cortex[15,16], entopeduncular nucleus/globus pallidus[17,18], lateral preoptic area (LPO) [29], ventral pallidum[19], lateral hypothalamus (LH/LHA) [20], ventromedial hypothalamus[16,21,22] , septum[23], central amygdala (CeA) [21], and bed nucleus of the stria terminalis (BNST)[21]. It also receives reciprocal inputs from the VTA[24], laterodorsal tegmental nucleus[25], periaqueductal gray (PAG)[15,16], and locus coeruleus[1,15] forming complex feedback loops that modulate activity. Given the widespread expression of various G protein-coupled receptors on LHb neurons and their afferents, LHb neuronal activity is subject to neuromodulatory actions of both fast and slow synaptic transmission from glutamate and GABA, as well as other neurotransmitters and neuromodulators including endocannabinoids[26], acetylcholine[27], serotonin[28-30], norepinephrine[31] and several co-released neuropeptides such as orexin[8], neuropeptide Y[32,33], dynorphin[16,34] and corticotropin-releasing factor (CRF)[35-38]. These

92 diverse glutamatergic, GABAergic, and neuromodulatory signals provide the LHb with
93 information related to motivation, reward, aversion, and stress.
94 Specifically regarding CRF neuromodulatory actions, hypothalamic (paraventricular
95 nucleus of hypothalamus, PVH) and extra-hypothalamic CRF systems mediate stress
96 responses, and their dysfunction is implicated in stress-related disorders. CRF's central
97 action through its receptors CRFR1/2 (both G protein-coupled receptors) is cell type-,
98 region- and pathway-specific and depends on prior stress exposure[39]. Additionally, sex
99 differences in CRF signaling may contribute to female vulnerability to anxiety and
100 depression[40]. Our previous studies demonstrated that the rodent LHb is highly
101 responsive to CRF[35,36,38], increasing LHb neuronal excitability via CRFR1-PKA-
102 dependent suppression of different potassium currents (small conductance potassium
103 SK channels in rat LHb[38]; M-type potassium channels in mouse LHb[35]). In rat LHb, CRF
104 reduces presynaptic GABA release via retrograde endocannabinoid signaling, without
105 changing glutamatergic activity, whereas in mouse LHb, CRF attenuates both
106 GABAergic and glutamatergic transmission[35,38]. We also showed that early life stress
107 and brain trauma augment endogenous LHb CRF-CRFR1 signaling, contributing to LHb
108 hyperexcitability[36,38].
109 Building on these findings, here we investigated the source of CRF inputs to the LHb
110 which remained unclear. Using viral-based Cre-mediated strategies in CRF transgenic
111 mouse lines, we mapped LHb-projecting CRF neurons and discovered a previously
112 uncharacterized neural subpopulation of LHb that expresses CRF (LHb^{CRF} neurons).
113 We then traced the major downstream targets of LHb^{CRF} axonal projections, revealing a
114 complex architecture of both local intra-habenular microcircuits and widespread long-

range projections. Our mapping identified LHb^{CRF} terminals across multiple brain regions, including diencephalic regions such as the LH/LHA and zona incerta (ZI), as well as critical midbrain and hindbrain centers involved in defense and motivation, such as the PAG, superior colliculus (SC), VTA, and RMTg. For the initial characterization of behavioral relevance of these neurons, we employed a chemogenetic gain-of-function strategy using Gq-DREADDs. This approach was specifically chosen over inhibition because chemogenetic silencing of major LHb projection targets such as the VTA and RMTg often fail to modulate baseline behaviors like locomotion or anxiety unless the animal is specifically challenged by a stressor[15]. Furthermore, given that the chemogenetic activation of other distinct LHb subpopulations, such as Pituitary Adenylate Cyclase-Activating Polypeptide (PACAP)-expressing neurons, has been shown to paradoxically produce rewarding effects and decrease fear[41], we sought to determine the specific valence and behavioral impact of the LHb^{CRF} population upon their activation. We utilized a battery of assays including the Open Field Test (OFT), Elevated Zero Maze (EZM), and Light-Dark Task (LDT) as critical controls to ensure that chemogenetic activation of LHb^{CRF} neurons did not simply induce generalized anxiety or motor deficits. To test the role of these neurons in motivated and defensive states, we employed Conditioned Place Preference (CPP) and the Visual Looming Shadow Test (VLST). Specifically, the VLST was chosen for the assessment of innate defensive behaviors, as hypothalamic CRF neurons and LHb neurons have been shown to play a significant role in the modulation of this behavior [42-45]. Our results reveal that LHb^{CRF} neurons may play a specific role in innate threat-evoked defensive behaviors, characterized by increased frequency and duration of action-locking behaviors and sex-

138 dependent differences in escape latencies and post-escape safety-seeking upon
139 chemogenetic activation. We also identified significant sexual dimorphism in the
140 population size, basal excitability, and local excitatory connectivity of LHb^{CRF} neurons.
141 These findings suggest that while both sexes exhibit an increased adoption of action-
142 locking behaviors upon LHb^{CRF} circuit activation, they may do so through potentially
143 divergent cellular and synaptic mechanisms. Specifically, the higher absolute number
144 and increased intrinsic excitability of LHb^{CRF} neurons in males, contrasted with the
145 significantly stronger local synaptic gain observed in females, may contribute to the
146 observed sex-dependent variations in escape latency and post-escape safety-seeking
147 behavior.
148

149 **Results**

150 In the present study, we used CRH-Cre::Ai14 or CRH-Cre::Ai6 reporter lines in
151 conjunction with the standard CRH-Cre line to facilitate the specific identification and
152 visualization of CRF+ neurons for our RNAscope, electrophysiology, local circuit
153 mapping as well as chemogenetic and optogenetic experiments. It is important to note
154 that all three lines utilize the same Cre-driver to target the CRF population; the reporter
155 lines (Ai14/Ai6) simply offer the technical advantage of endogenous fluorophore
156 expression (tdTomato or ZsGreen) upon Cre-mediated recombination. Extensive
157 literature has validated that these Cre-dependent reporter strains reliably recapitulate
158 the expression patterns of the underlying Cre-driver line without altering the
159 physiological or behavioral characteristics of the target neuronal population [46,47].
160 Specifically, the CRH-Cre line has been widely demonstrated to target CRF neurons

with high specificity and efficiency across various brain regions, and the addition of the Ai reporter alleles does not introduce confounding variables in behavioral responses[45,48-52].

A subpopulation of CRF projections to the LHb originates within the LHb itself. To identify CRF projections to the LHb, we used Cre-dependent retrograde viral tracing by bilaterally injecting retrograde adeno-associated virus (rgAAV-DIO-YFP) into the LHb of CRH-Cre male and female mice (n=3, Figure 1 and Supplementary Figure 1). This revealed an intrinsic subpopulation of LHb neurons expressing CRF (LHb^{CRF}). Beyond this local population, our mapping identified several prominent long-range CRF-expressing inputs:

- Primary Afferents: High densities of retrogradely labeled CRF+ cell bodies were observed in the pretectal area (PRT), the paraventricular nucleus of the thalamus (PVT), and the PAG.
- Secondary Midbrain Inputs: Substantial labeling was also identified in the midbrain reticular nucleus (MRN) and SC.
- Hypothalamic and Limbic Contributions: Smaller but consistent populations of CRF+ neurons were detected in the PVH, posterior hypothalamus (PH), LH/LHA, BNST, and LPO.

To determine if LHb^{CRF} neurons constitute a subclass of LHb^{PV} neurons, we also performed anti-parvalbumin immunostaining on retrogradely labeled LHb^{CRF} neurons. The absence of detectable parvalbumin expression in LHb^{CRF} neurons indicates that these may constitute distinct subpopulations, separate from LHb^{PV} neurons. (Supplementary Figure 2).

184

185 **LHb^{CRF} Neurons express VGLUT2 and GAD2 with a minority expressing vGAT**
186 **mRNA.**

187 To characterize the neurochemical identity of LHb^{CRF} neurons, we performed a
188 comprehensive, large-scale RNAscope experiment utilizing Zeiss AxioScan imaging
189 and QuPath automated analysis (Supplementary Figure 3), across the rostrocaudal axis
190 spanning five AP levels. While we initially attempted to utilize a Crh probe, technical
191 limitations regarding non-specific binding led us to utilize CRH-Cre::Ai14 mice, where
192 the tdTomato reporter identifies CRF+ neurons. Our data (Figures 2–3 and
193 Supplementary Figures 3–7) suggest that LHb^{CRF} neurons are primarily concentrated in
194 the rostral portion of the LHb (Bregma -1.06 to -1.34 mm, Figures 2-3 and
195 Supplementary Figures 4–7). Within these levels, the population exhibits a distinct
196 spatial organization: a dense cluster is situated in the medial LHb (LHbM), bordering the
197 medial habenula, while a significant subpopulation extends into the lateral LHb (LHbL).
198 As the axis moves caudally (Bregma -1.58 mm, Supplementary Figures 6-7), the
199 population density decreases significantly. To ensure our quantification was not
200 confounded by potential structural dimorphism, we analyzed the total surface area of
201 the LHb across all five AP levels using the Allen Brain Atlas and Paxinos templates. We
202 identified a total of 1,388 CRF+ cells across 13 mice (n = 833 in 7 males; n = 555 in 6
203 females). We found no significant differences in LHb surface area between sexes
204 (Supplementary Figure 3; $F(1, 55) = 1.924$, $p = 0.17$, 2-way ANOVA), allowing for an
205 unbiased comparison of cell counts. Our results show that while the topographical
206 distribution is identical between sexes, male mice possess a significantly higher

207 absolute number of LHb^{CRF} neurons than females (Figure 4; Student's t-test, $p < 0.05$).
208 We further characterized these cells by their transcriptional profile, confirming that 100%
209 express VGLUT2. Approximately 17–18% co-express GAD2, while a negligible minority
210 (2–5%, primarily in males) co-express vGAT and VGLUT2 (Figure 4; Chi-Square test, p
211 < 0.01). These findings identify LHb^{CRF} neurons as a predominantly VGLUT2+
212 subpopulation with some co-expressing GAD2+ and a significant sex-dependent
213 variations in total population size.
214

215 **LHb^{CRF} neurons provide both local and long-range projections.**

216 To characterize the anatomical outputs of the LHb^{CRF} population, we mapped their
217 efferent projections using AAV5-Syn-FLEX-ChrimsonR-tdTomato in CRH-Cre::Ai6 mice
218 of both sexes (Figures 5-6). We utilized ChrimsonR because its red-shifted excitation
219 spectrum offers superior tissue penetration and reduced light scattering compared to
220 traditional blue-light-activated opsins, providing a significantly more robust platform for
221 mapping distal terminal fields[53,54]. The integration of the Ai6 reporter line allowed us to
222 rigorously validate our targeting specificity by confirming that ChrimsonR-tdTomato
223 expression was strictly restricted to GFP-labeled CRF+ neurons within the LHb
224 boundaries. Utilizing high-resolution Zeiss AxioScan microscopy, this standardized
225 approach enabled the identification of LHb^{CRF} axonal projections within the LHb itself,
226 as well as several key long-range targets.These distal projections included the LH/LHA,
227 ZI, SC, PAG, VTA, substantia nigra pars compacta (SNC), as well as the dorsal raphe
228 (DR), RMTg, and median raphe (MnR). These projection patterns were observed across
229 both male and female mice (Figures 5–6). Our findings were further validated using two

230 additional anterograde tracing strategies in males (AAV8-DIO-mCherry) and females
231 (AAV5-EF1a-ChR2-EYFP). These complementary methods confirmed the axonal
232 projections identified by our ChrimsonR approach within the LHb and major midbrain
233 structures, including the RMTg, PAG, and SNC (Supplementary Figures 8-9). Together,
234 these data establish that LHb^{CRF} neurons form a widespread network reaching multiple
235 diencephalic, midbrain, and hindbrain centers.
236

237 **Behavioral correlates of LHb^{CRF} neuronal activity**

238 To establish causal links between LHb^{CRF} neuronal activity and behavior, we employed
239 a Cre-dependent chemogenetic approach using excitatory Designer Receptors
240 Exclusively Activated by Designer Drugs (DREADDs). Mice across multiple cohorts
241 underwent behavioral testing (7-day intervals) in one of two sequences: light-dark test
242 (LDT) followed by elevated zero maze (EZM), or open field test (OFT) followed by
243 conditioned place preference (CPP) and then visual looming shadow test (VLST). The
244 inclusion of EZM, LDT, and OFT was crucial for interpreting CPP and VLST data by
245 controlling for potential non-specific effects of Gq-DREADD activation of LHb^{CRF}
246 neurons on locomotion and general anxiety. To selectively activate LHb neurons
247 expressing CRF, we employed a Cre-dependent chemogenetic approach using two
248 different constructs of DREADDs. In adult male and female CRH-Cre mice (postnatal
249 day 42 [P42]), we performed bilateral stereotaxic injections into the LHb of an adeno-
250 associated viral (AAV) vector encoding an excitatory Gq-coupled DREADD. Specifically,
251 we utilized AAV8-hSyn-DIO-hM3D(Gq)-mCherry in CRH-Cre mice to drive Cre-
252 dependent expression of hM3D(Gq) tagged with mCherry (Supplementary Figure 10).

253 Given the expression of the tdTomato reporter in CRH-Cre::Ai14 mice, we used an
254 alternative Cre-dependent viral construct, AAV8-hSyn-DIO-HA-hM3D(Gq)-IRES-
255 mCitrine, to avoid spectral overlap and ensure clear visualization of DREADD-
256 expressing cells (Figure 7). To activate LHb^{CRF} neurons expressing Gq-DREADDs in
257 CRH-Cre or CRH-Cre::Ai14 mice, mice received i.p. injections of 0.3mg/kg JHU37160
258 or vehicle (saline) 30 min prior to behavioral assay, at least four weeks post-surgery
259 (consistent with our previous study[55]). During CPP conditioning, mice received
260 JHU37160 or saline prior to the second of two daily conditioning sessions (days 2-3),
261 but not during baseline evaluation (day 1) or testing (day 4). We confirmed that Gq-
262 DREADD expression was restricted to the LHb^{CRF} neurons by mCherry expression
263 (Supplementary Figure 10B) or HA-hM3Dq immunostaining (Figure 7C-E) and that bath
264 application of JHU37160 (100nM) significantly increased neuronal excitability of LHb^{CRF}
265 neuron expressing DREADD construct (Figure 7B).
266 **Chemogenetic activation of LHb^{CRF} neurons did not induce anxiety-like or risk-**
267 **taking behaviors.** In EZM and LDT, mice generally prefer to spend more time in the
268 closed arms of the EZM or the dark chamber of the LDT box. However, they may also
269 be motivated to explore the open arms of the EZM or the bright area of the LDT
270 apparatus. Increased exploration of the open arms and light chamber is believed to
271 reflect lower anxiety/more novelty seeking/risk-taking behaviors in mice. As shown in
272 example traces of automated tracking of mouse movement in the EZM and LDT in
273 Supplementary Figure 10C-D, activation of LHb^{CRF} neurons by JHU37160 in CRH-Cre
274 mice expressing Gq-DREADD did not alter time spent in the open arms of EZM or the
275 light chamber of LDT [Supplementary Figure 10E-G, EZM: Male (n=5-7/group); arm

effect: F (1, 20) = 280.1, p<0.0001, JHU37160 effect: F (1, 20) = 0.031, p=0.86, arm x JHU37160 interaction: F (1, 20) = 0.34, p=0.56; Supplementary Figure 10H-J, EZM: Female (n=5-6/group); arm effect: F (1, 18) = 30.39, p<0.0001, JHU37160 effect: F (1, 18) = 0.00039, p=0.98, arm x JHU37160 interaction: F (1, 18) = 0.35, p=0.55; Supplementary Figure 10K-M, LDT: Male (n=5-7/group); chamber effect: F (1, 20) = 98.61, p<0.0001, JHU37160 effect: F (1, 20) = 0.07734, p=0.78, chamber x JHU37160 interaction: F (1, 20) = 0.34, p=0.56; Supplementary Figure 10O-P, LDT: Female (n=5-6/group); chamber effect: F (1, 18) = 34.68, p<0.0001, JHU37160 effect: F (1, 18) = 9.026e-005, p=0.99, chamber x JHU37160 interaction: F (1, 18) = 1.266, p=0.27, two-way ANOVA].

Chemogenetic activation of LHb^{CRF} neurons did not induce CPP. To control for Gq-DREADD effects on locomotor activity and general anxiety with EZM and LDT in CRH-Cre::Ai14 lines, we performed OFT where we consistently observed that chemogenetic excitation of LHb^{CRF} neurons by JHU37160 in CRH-Cre::Ai14 mice did not affect locomotor activity or promote anxiety-like behaviors in the OFT in either sex as shown in example traces in Figure 7F-G. CRH-Cre::Ai14 mice expressing Gq-DREADD injected with either JHU37160 or saline spent significantly less time in the center of the apparatus compared to the edges (periphery) and their total distance traveled was not altered by our chemogenetic manipulation [Figure 7J-K, OFT: Male (n=10-12/group); region effect: F (1, 40) = 6656, p<0.0001, JHU37160 effect: F (1, 40) = 0.000, p=0.99, region x JHU37160 interaction: F (1, 40) = 0.018, p=0.89; Figure 7L-M, OFT: Female (n=9-10/group); region effect: F (1, 34) = 4476, p<0.0001, JHU37160 effect: F (1, 18) = 0.000, p=0.99, region x JHU37160 interaction: F (1, 34) = 0.5729, p=0.45, two-way

299 ANOVA]. We then performed CPP to evaluate whether chemogenetic activation of
300 LHb^{CRF} neurons is rewarding. We found that CRH-Cre::Ai14 mice expressing Gq-
301 DREADD injected with JHU37160 during place conditioning spent equal time in
302 JHU37160-paired and unpaired sides as seen in CRH-Cre::Ai14 mice expressing Gq-
303 DREADD that received only saline during conditioning (Figure 7H-I and 7N,O).
304 **Chemogenetic activation of LHb^{CRF} neurons increased passive action-locking**
305 **behavioral responses to threat.** Finally, we tested whether chemogenetic activation of
306 LHb^{CRF} neurons biases threat-evoked responses towards active (escape) or passive
307 (action-locking/freezing) defensive behaviors and further assessed how this activation
308 influences the temporal dynamics of these responses, including escape latency, action-
309 locking duration, and post-escape shelter stayin mice (Figure 8). In CRH-Cre::Ai14 mice
310 expressing Gq-DREADDs, administration of JHU37160 (0.3 mg/kg) significantly
311 increased the frequency and duration of passive action-locking/freezing responses in
312 both males and females compared to saline-treated controls (Figure 8B: effect of
313 JHU37160: $p < 0.05$, Chi-squared tests; 10C: JHU37160 effect: $F (1, 31) = 8.027$, $p <$
314 0.01, sex effect: $F (1, 31) = 0.2792$ $p=0.601$, JHU37160 x sex interaction: $F (1, 31)$
315 $= 0.1724$, $p=0.68$). Interestingly, we observed that activation of LHb^{CRF} neurons
316 significantly prolonged the latency to initiate escape in male mice but had no such effect
317 in females (Figure 8D; JHU37160 effect: $F(1, 35) = 9.030$, $p < 0.01$; sex effect: $F(1, 35)$
318 $= 0.062$, $p = 0.80$; JHU37160 x sex interaction: $F(1, 35) = 3.805$, $p = 0.05$). Further
319 analysis revealed sex-specific differences in post-threat behavior. Gq-activation in
320 females resulted in a significantly prolonged stay within the shelter following escape
321 (Figure 8E; JHU37160 effect: $F (1, 34) = 1.707$, $p=0.2001$; sex effect: $F (1, 34) = 6.192$,

322 $p<0.05$; JHU37160 x sex interaction: $F(1, 34) = 7.991$, $p<0.01$). Collectively, these
323 findings demonstrate that LHb^{CRF} neurons selectively increase the prevalence and
324 duration of passive defensive strategies in both sexes, with sex-specific effects
325 manifesting as differences in escape latency and shelter-seeking duration.
326
327 **LHb^{CRF} neurons exhibit higher baseline spontaneous activity in male mice**
328 **compared to female mice.**
329 To further investigate baseline physiological differences in **LHb^{CRF}** activity, , we further
330 evaluated basal levels of spontaneous activity and neuronal excitability of LHb^{CRF}
331 neurons (labeled with tdTomato) in CRH-Cre::Ai14 male and female mice (Figure 9A).
332 We observed that male LHb^{CRF} neurons exhibited higher levels of spontaneous activity
333 with more LHb^{CRF} neurons in tonic and bursting mode of activity than female LHb^{CRF}
334 neurons (Figure 9B). In contrast, LHb^{CRF} neuronal excitability in response to
335 depolarization did not differ between male and female CRH-Cre::Ai14 mice (Figure 9C)
336 (Figure 9B, male: n=49 cells/22 mice, female: n=41 cells/9 mice in pie charts, *$p<0.05$,
337 Chi squared tests; Figure 9C, male: n=42 cells/22 mice, female: n=30 cells/9 mice in
338 excitability, effect of sex: $F(1, 740) = 0.096$, $p=0.75$, 2-way ANOVA).
339 **LHb^{CRF} neurons in females form stronger local excitatory connections within the**
340 **LHb.**
341 To functionally validate our anterograde tracing and confirm the existence of a local
342 microcircuit, we employed an optogenetic approach in CRH-Cre::Ai6 mice. By injecting
343 AAV5-Syn-FLEX-ChrimsonR-tdTomato into the LHb, we specifically targeted and
344 excited LHb^{CRF} neurons, identifying them via endogenous GFP labeling (Figure 10A–B).

345 We performed whole-cell patch-clamp recordings from neighboring GFP-negative (non-
346 CRF) neurons while optically stimulating ChrimsonR-expressing CRF+ cells and their
347 local terminals. These experiments revealed robust light-evoked excitatory postsynaptic
348 currents (oEPSCs), providing functional evidence of a direct intra-habenular
349 glutamatergic microcircuit. We verified that these connections are monosynaptic, as the
350 application of TTX abolished most of the oEPSCs, while subsequent 4-AP treatment
351 recovered the currents nearly to baseline levels (Figure 10C). Recordings at a holding
352 potential of +10 mV (the reversal potential for AMPA and NMDA receptor-mediated
353 currents) showed no detectable oIPSCs or oEPSCs. However, at +40 mV, mixed
354 oEPSCs were reliably evoked in both male and female mice (Figure 10D–E).Our
355 optogenetic dissection further revealed that this local circuitry is sexually dimorphic.
356 While the raw input/output (I/O) curves across varying LED intensities showed no
357 significant difference between sexes (Figure 10F; sex effect: $F(1, 242) = 0.071$, $p =$
358 0.789), normalized data, which controlled for variability in viral expression by scaling
359 responses between minimum and maximum synaptic values, revealed a significant
360 leftward shift in females (Figure 10G; sex effect: $F(1, 242) = 11.27$, $p < 0.001$). This
361 indicates that female LHb^{CRF} neurons form significantly stronger local excitatory
362 connections than their male counterparts. This enhanced synaptic gain in females is
363 driven by a higher probability of presynaptic glutamate release, as evidenced by a
364 significantly lower paired-pulse ratio (PPR) compared to males (Figure 10H; sex effect:
365 $F(1, 190) = 16.23$, $p < 0.0001$). In contrast, we found no sex differences in the
366 AMPA/NMDA ratio (Figure 10I; $p = 0.975$), suggesting that this sexual dimorphism is
367 mediated by presynaptic release dynamics rather than differences in postsynaptic

368 receptor composition or plasticity. Collectively, these data establish a high-gain local
369 excitatory drive in females that may underlie their distinct behavioral responses to
370 threat.

371 **Discussion**

372 The LHb's broad involvement in various adaptive behaviors and neuropsychiatric
373 disorders, including depression, schizophrenia, Parkinson's disease, and attention-
374 deficit hyperactivity disorder, continues to fuel significant clinical interest[56-64]. Despite
375 displaying relatively uniform electrophysiological properties, LHb neurons exhibit
376 substantial heterogeneity in their transcriptional profiles, afferents, and
377 projections[6,7,65,66]. Furthermore, neuromodulation profoundly shapes LHb neuronal
378 activity through mechanisms such as the synaptic co-release of multiple
379 neuromodulators alongside neurotransmitters, the expression of diverse
380 neuromodulatory receptors, and the integration of various neuromodulatory signals,
381 potentially contributing to the functional specializations of distinct LHb neuron
382 subpopulations[2]. Given this less explored facet of LHb function, and building on our
383 previous demonstration of the LHb's responsiveness to the key stress neuromodulator
384 CRF[35,36,38], we specifically investigated the origin of these previously uncharacterized
385 CRF inputs to the LHb. Our investigation revealed several brain regions including a
386 distinct subpopulation of LHb neurons that express CRF (LHb^{CRF}). LHb^{CRF} neurons
387 universally co-express VGLUT2. Within this population, we identified a notable subset of
388 VGLUT2+/GAD2+ neurons , which together could serve as a source of both local intra-
389 habenular microcircuits and widespread distal neuromodulatory inputs to downstream
390 targets. Using gain-of-function chemogenetic strategies, we further demonstrate that

391 LHb^{CRF} neurons may play a pivotal role in biasing behavioral selection toward passive
392 defensive responses (i.e., action-locking behaviors in VLST). While this effect is
393 observed across both sexes, our findings suggest that sexually dimorphic cellular and
394 synaptic mechanisms may underlie these shared passive behavioral outputs, while also
395 driving distinct sex differences in the temporal dynamics of the response.
396 Retrograde mapping in adult CRH-Cre mice identified the PRT, PAG, PVT, and the LHb
397 itself as the primary sources of CRF inputs to the LHb. These major drivers are
398 complemented by significant contributions from the MRN and SC, as well as consistent
399 inputs from the PVH, PH, LH/LHA, BNST, and LPO. While many of these pathways
400 including local intra-habenular microcircuits and long-range limbic inputs are well-
401 documented[1,2,9,11,67-70], the recently identified PVT-LHb connection specifically highlights
402 the evolving understanding of thalamic influence on this region. Notably, we found no
403 existing literature documenting a direct connection between the PRT and the LHb,
404 suggesting this may be a previously uncharacterized pathway[69]. We acknowledge that
405 our retrograde strategy likely provides a conservative or "limited view" of the total CRF
406 inputs, as certain pathways may be less amenable to retrograde transduction via rgAAV
407 vectors. The lack of prior anatomical evidence for the PRT-LHb connection underscores
408 the need for further investigation to validate this finding and explore the functional role
409 of these PRT^{CRF} neurons in LHb-mediated behaviors.
410
411 We then specifically focused on the newly discovered subpopulation of CRF-
412 expressing LHb neurons (LHb^{CRF}), mapping their axonal projection targets and
413 characterizing their physiological and behavioral profiles in both sexes. Our RNAscope

414 analysis revealed that these neurons are primarily concentrated in the rostral LHb,
415 exhibiting a distinct spatial organization: a dense cluster resides in the medial LHb
416 (LHbM) bordering the medial habenula, while a significant subpopulation extends into
417 the lateral LHb (LHbL). While this topographical distribution is identical between sexes,
418 we found that males possess a significantly higher absolute number of LHb^{CRF} neurons
419 than females. Transcriptional profiling confirmed that 100% of these neurons express
420 VGLUT2. Approximately 17-18% co-express GAD2, while only a negligible minority
421 (primarily in males) co-express vGAT. Crucially, our optogenetic data provides
422 functional evidence for this excitatory topography; light-evoked currents recorded from
423 local non-CRF neurons confirmed that these rostral LHb^{CRF} neurons form a functional
424 intra-habenular circuit, with females exhibiting significantly stronger synaptic
425 connections. Notably, although a GAD2+/VGLUT2+/vGAT- population has been
426 reported to provide local inhibition within the LHb[8], our functional experiments
427 demonstrated that stimulation of LHb^{CRF} neurons evoked purely glutamatergic oEPSCs
428 in local targets with no detectable inhibitory component. This suggests that the GAD2-
429 expressing LHb^{CRF} subset likely corresponds to the distinct excitatory class recently
430 defined by Quina et al. (2020), which serves as a glutamatergic output pathway to the
431 mesopontine tegmentum[71]. Therefore, we conclude that the LHb^{CRF} population is
432 functionally excitatory, and the GAD2-positive fraction likely contributes to long-range
433 excitatory projections rather than local inhibition. While a minor fraction of VGLUT2+
434 LHb^{CRF} neurons were found to be vGAT+/GAD2-, potentially providing an inhibitory
435 substrate (particularly in males), we did not encounter these functional connections in
436 our recordings, as no inhibitory currents were observed. Regarding our synaptic

437 validation, it is of note that TTX did not completely abolish oEPSCs. While this treatment
438 typically blocks all mono- and polysynaptic currents, the use of ChrimsonR can result in
439 sufficient terminal depolarization to trigger neurotransmitter release even in the absence
440 of action potentials, leaving a small residual oEPSC. Nevertheless, the recovery of the
441 majority of the oEPSC amplitude following 4-AP treatment confirms the monosynaptic
442 nature of this excitatory circuit.
443 Complementing this local microcircuitry, our anterograde tracing studies identified
444 widespread LHb^{CRF} axonal projections not only within the LHb but also to several key
445 long-range targets. These distal projections include hypothalamic/thalamic structures
446 including LH/LHA and ZI, midbrain structures including SC, PAG, VTA and SNC and
447 hindbrain including DR, RMTg, and MnR. Notably, all of these regions have been
448 previously reported as primary output targets of LHb neurons in male and female
449 mice[2,69,70,72]. Collectively, this diverse projection profile, paired with a potent local
450 excitatory microcircuit, positions LHb^{CRF} neurons as a central hub capable of
451 orchestrating complex behavioral and physiological responses through widespread
452 influence on midbrain and hindbrain nuclei.
453 The expression of VGLUT2 in LHb^{CRF} neurons, coupled with the lack of parvalbumin
454 expression, could indicate that LHb^{CRF} neurons are a distinct subpopulation separate
455 from LHb^{PV} neurons. This finding also excludes the possibility that LHb^{CRF} neurons are
456 a component of the LHb^{PV} GABAergic interneurons responsible for local inhibition of
457 glutamatergic neurons[11]. Our future research will focus on determining whether the
458 intrinsic and extrinsic axonal terminals of LHb^{CRF} neurons co-release glutamate and
459 CRF to modulate synaptic transmission within the LHb and its distal downstream

460 targets. Furthermore, we aim to elucidate the specific behavioral significance of these
461 dual-transmitter circuits in the context of stress and defensive strategies.
462 Our chemogenetic investigation reveals a role for LHb^{CRF} neurons in biasing behavioral
463 selection toward passive strategies, specifically increasing the frequency and duration
464 of action-locking/freezing in response to looming threats in both sexes. However, the
465 temporal execution of these defenses is strikingly dimorphic: Gq-activation prolonged
466 escape latencies in males, whereas in females, it resulted in a protracted post-escape
467 shelter stay. This increased shelter occupancy in females likely reflects heightened fear
468 levels or a persistent perception of threat, necessitating a longer period to re-establish a
469 sense of safety before re-emerging[43].
470 Our data also suggests that these distinct behavioral phenotypes may be driven by
471 divergent physiological strategies. While males possess a significantly higher absolute
472 number of LHb^{CRF} neurons and higher basal spontaneous activity characterized by
473 increased tonic and bursting firing modes, their local synaptic connections are less
474 efficient than those in females. In contrast, female LHb^{CRF} neurons exhibit lower intrinsic
475 excitability but form more potent local excitatory connections, characterized by a higher
476 probability of glutamate release (lower PPR).
477 This enhanced local synaptic gain in females likely provide the physiological substrate
478 for their prolonged action-locking and persistent shelter-seeking behavior. We propose
479 that the lower intrinsic excitability observed in females may represent a homeostatic
480 compensatory response to this high-gain synaptic drive, maintaining circuit stability.
481 Conversely, the behavioral effects in males may rely on a higher population-level output
482 and a higher baseline firing rate.

483 Intriguingly, while basal spontaneous activity differed between sexes, we found no sex-
484 specific differences in overall neuronal excitability in response to direct depolarization.
485 This discrepancy may be explained by the high proportion of bursting neurons in males.
486 Because bursting neurons typically elicit fewer action potentials per depolarization
487 compared to tonically active neurons during excitability protocols, the prevalence of this
488 firing mode in males likely offsets their higher tonic activity, resulting in similar
489 aggregate excitability levels across sexes.
490 While we have yet to dissect the specific synaptic weights of LHb^{CRF} projections to distal
491 targets (e.g., PAG or RMTg), it is highly probable that these sex-dependent differences
492 in population size, baseline firing, and local synaptic gain collectively dictate the distinct
493 behavioral outcomes observed under threat.
494 The hypothalamic PVH and specific extrahypothalamic CRF neurons, including the
495 BNST (which we found both to provide weak CRF projections to the LHb), are
496 implicated in threat-driven defensive behaviors[73]. The looming shadow test also
497 underscores the critical involvement of both LHb neurons[44] and PVN^{CRF} neurons[43] in
498 threat-provoked defensive responses. This test exhibits strong face validity as the active
499 fleeing (flight) or passive staying (action-locking/freezing) behaviors observed closely
500 resemble human reactions to imminent danger. Importantly, dysregulation of these
501 defensive mechanisms, such as rigid and persistent freezing or escape, and prolonged
502 threat reactivity, are also key features of stress-related psychopathologies like anxiety
503 and PTSD[74-79].
504 Fiber photometric recordings of PVN^{CRF} neurons in the looming shadow test
505 demonstrated that augmented PVN^{CRF} neuronal activity precedes escape responses

506 elicited by a looming or advancing threat[43]. Moreover, optogenetic inhibition of PVN^{CRF}
507 neurons attenuates escape behavior[43]. Consequently, these findings suggest that
508 PVN^{CRF} activity encodes an anticipatory or preparatory signal for the initiation of
509 escape. Furthermore, distinct subpopulations of LHb neurons are involved in either
510 predicting or reflecting the selection and execution of threat-driven action-locking or
511 escape behaviors in the looming shadow test[44]. Fiber photometry of LHb population
512 activity revealed an increase in calcium signal time-locked with escape and a decrease
513 time-locked with action-locking. However, miniscope calcium imaging with single-cell
514 resolution uncovered distinct LHb neuronal clusters: some increase their activity before
515 and during escape while others decrease their activity before action-locking, while
516 others increase activity before action-locking while decreasing activity before escape.
517 The former outcome is reminiscent of PVN^{CRF} neuron activity during this test. Our
518 results suggest the possibility that LHb^{CRF} neurons represent a functionally distinct LHb
519 subpopulation that may encode action-locking defensive behaviors in response to an
520 imminent threat. Future miniscope calcium imaging studies can further elucidate the role
521 of LHb^{CRF} neurons and other LHb-projecting CRF neurons in the selection and
522 execution of appropriate defensive responses. Our previous work also demonstrated
523 that mild traumatic brain injury (mTBI) in male and female mice shifts threat responses
524 towards action-locking in the looming shadow test, and prolongs escape latency in
525 female mice specifically[36]. Considering that mTBI-induced LHb hyperactivity is partly
526 driven by an increase in CRF-CRFR1 signaling within the LHb in both sexes, it is crucial
527 to investigate how LHb^{CRF} circuits contribute to the altered defensive behaviors
528 observed after mTBI. Overall, our findings highlight that LHb^{CRF} neuronal activation

529 shifts mouse defensive behaviors towards action-locking in both sexes. However, this
530 activation produces distinct temporal profiles: it delays defensive reactions (increased
531 escape latency) in males and heightens fear responses (prolonged shelter stay) in
532 females. These findings suggest that while the core behavioral output, passive action-
533 locking, is shared, the underlying temporal execution and post-threat recovery may be
534 governed by sex-specific LHb^{CRF} circuit dynamics.
535 Curiously, our chemogenetic activation of LHb^{CRF} neurons did not alter place preference
536 in either sex while activation of distinct subpopulations of CRF neurons could exert
537 either place preference (e.g., NAc^{CRF} or CeA^{CRF} neurons) or aversion (e.g., $BNST^{CRF}$)[80].
538 One limitation of chemogenetic activation with sustained activation of LHb^{CRF} neurons is
539 its lack of the millisecond-scale temporal precision offered by optogenetics. This
540 limitation hinders a clear understanding of the immediate behavioral response to LHb^{CRF}
541 neuronal stimulation. Therefore, future studies using behavioral assays like the real-time
542 place preference paradigm could better address whether LHb^{CRF} neuronal stimulation
543 evokes aversive (avoidance) or appetitive (approach) motivation.
544 In summary, our work has unveiled a previously uncharacterized subpopulation of
545 LHb^{CRF} neurons that form both local microcircuits and long-range projections to the
546 midbrain and hindbrain. Our findings establish the LHb^{CRF} population as a novel,
547 sexually dimorphic component of the LHb's heterogeneous circuit architecture that
548 could bias defensive strategies toward action-locking under threat and may underlie the
549 sex-dependent variations in escape latency and post-escape shelter seeking observed
550 during the VLST. Further characterizing the precise functional connectivity and
551 behavioral contributions of these neurons based on their unique projection targets

552 represents a significant and timely direction for the field. Given that CRF
553 neuromodulation is inherently cell-type, region, and pathway-specific, dissecting these
554 distinct LHb^{CRF} circuits will provide essential insights into the nuanced mechanisms by
555 which CRF orchestrates complex behavioral states and sex-specific stress responses.

556 **Methods**

557 **Animals**

558 Male and female mice, aged 9-13 weeks, were used for all experiments (viral injections
559 at postnatal day 42 (P42); experiments commencing at 9 weeks of age). All procedures
560 adhered to the NIH Guide for the Care and Use of Laboratory Animals and the ARRIVE
561 guidelines 2.0, and were approved by the Uniformed Services University Institutional
562 Animal Care and Use Committee. The following mouse strains were used: CRH-ires-
563 CRE (B6(Cg)-*Crh*$^{tm1(cre)Zjh}$/J, Strain #: 012704), n = 32; CRH-Cre::Ai14 [generated by
564 crossing homozygous CRH-ires-Cre mice (n=16 breeders) with Ai14 Cre reporter mice
565 (n=12 breeders)(B6.Cg-*Gt(ROSA)26Sor*$^{tm14(CAG-tdTomato)Hze}$/J, Strain #: 007914)] or Ai6
566 Cre reporter mice (n=4 breeders) (B6.Cg-*Gt(ROSA)26Sor*$^{tm6(CAG-ZsGreen1)Hze}$/J, Strain#:
567 :007906), reporter lines (n=101), total n = 165. Mice were acquired from Jackson
568 Laboratories at P35-P49 and allowed at least 72 hours of acclimation before
569 experimental procedures began. Different numbers of male and female mice were used
570 due to stock availability from the supplier and in-house breeding. For chemogenetic
571 experiments, animals were randomly assigned to groups, and all data acquisition and
572 analysis were performed by investigators blinded to the group assignments
573 (Gq+saline/Gq+JHU37160). Seven mice were excluded from chemogenetic studies due
574 to incorrect LHb targeting. Mice were group-housed in standard cages under a

575 12hr/12hr light-dark cycle with standard laboratory lighting conditions (lights on, 0600-
576 1800, ~200 lux), with ad libitum access to food and water. All procedures were
577 performed 2-4 hours after the start of the light cycle. All efforts were made to minimize
578 animal suffering and reduce the number of animals used throughout this study.

579 **Virus injections for retrograde and anterograde tracings and chemogenetics**

580 Mice (P42) were anesthetized with 1-3% isoflurane vaporized in oxygen and secured in
581 a stereotaxic frame. Body temperature was maintained at 37°C throughout the
582 procedure and during recovery using a heating pad. The scalp was shaved, and a
583 midline incision was made to expose the skull. The following viral vectors were
584 bilaterally injected into the LHb: rgAAV-EF1a-DIO EYFP (Addgene #27056), AAV5-Syn-
585 FLEX-rc[ChrimsonR-tdTomato (Addgene#62723), AAV5-Ef1a-DIO
586 hChR2(E123T/T159C)-EYFP (Addgene #35509), AAV8-hSyn-DIO-mCherry (Addgene
587 #50459), AAV8-hSyn-DIO-hM3D(Gq)-mCherry (Addgene #44361), AAV8-hSyn-DIO-
588 HA-hM4D(Gi)-IRES-mCitrine (Addgene #50455). Viral vectors (~50 nL/side) were
589 infused at a rate of 1nL/sec over 5 minutes using a Nanoject III Injector (Drummond)
590 and pulled glass pipettes into the LHb (coordinates from bregma: AP, -1.35 mm; ML,
591 ±0.5 mm; DV, -3.0 mm). The injection pipette was left in place for 5 minutes post-
592 infusion to allow for viral diffusion. During recovery (approximately 30-60 minutes), mice
593 were placed in a warm cage (heating pad beneath) or under a heating lamp to prevent
594 hypothermia. Post-operative care included continuous monitoring until purposeful
595 movement was regained. Animal health and weight were monitored and recorded for at
596 least 3 days post-surgery. Mice received a subcutaneous injection of 5 mg/kg carprofen
597 (for analgesia) immediately after surgery and were monitored daily for signs of pain,

598 with carprofen administered as needed. Viral expression was confirmed via
599 fluorescence and/or immunohistochemistry at the conclusion of behavioral experiments.
600 Mice lacking bilateral viral expression in the LHb were excluded from data analysis.

601 **In Situ Hybridization (RNAscope)**

602 Multiplex fluorescent *in situ* hybridization (FISH) was performed using the RNAscope
603 Fluorescent Multiplex Assay (Advanced Cell Diagnostics [ACD], Newark, CA) to detect
604 mRNA transcripts for *Slc17a6* (VGLUT2), *Slc32a1* (VGAT), and *Gad2* (GAD2).

605 **Tissue Preparation:** Male and female CRH-Cre::Ai14 mice were anesthetized with
606 ketamine/xylazine (85/10 mg/kg, i.p.) and transcardially perfused with 100 ml of 1x PBS
607 followed by 100 ml of 4% paraformaldehyde (PFA). Brains were post-fixed in 4% PFA
608 (24 h), cryoprotected in 20% sucrose (72 h), and frozen on dry ice. Coronal sections
609 (20μm) spanning the LHb (Bregma -0.94 to -2.30 mm; Paxinos and Franklin, 2007)
610 were collected via cryostat (Leica CM1900) and mounted on glass slides.

611 **Sequential Imaging and RNAscope Assay:** Because the endogenous tdTomato
612 signal is quenched during the RNAscope protease and dehydration steps, a sequential
613 imaging strategy was employed:

614 1. Pre-assay Imaging (Scan 1): Prior to the FISH assay, slides were scanned under
615 a 20x objective (Zeiss Axioscan) to capture the endogenous tdTomato (red)
616 signal from CRF+ neurons.
617 2. RNAscope Processing: Following Scan 1, coverslips were removed in 4x SSC,
618 and sections were washed in 1x PBS. Sections were baked at 60° C, post-fixed
619 in 4% PFA (1h at 4°C), and dehydrated in an ascending ethanol series. Following

620 hydrogen peroxide treatment and antigen retrieval, sections were treated with
621 Protease III.
622 3. Hybridization and Detection: Sections were incubated (2h at 40°C) with a
623 multiplex probe cocktail: *Slc17a6*-C1 (Cat# 319171), *Slc32a1*-C3 (Cat# 319191),
624 and *Gad2*-C4 (Cat# 439371). Signals were amplified using AMPs 1–3 and
625 developed with HRP-conjugated Vivid fluorophores (1:5000 dilution): Vivid 520
626 (*Slc17a6*), Vivid 570 (*Slc32a1*), and Vivid 650 (*Gad2*).
627 4. Post-assay Imaging (Scan 2): After signal development, sections were
628 counterstained and mounted with ProLong Gold with DAPI (Life Technologies). A
629 second scan was performed under identical settings to capture the FISH signals.
630 **Image Processing and Registration:** To visualize the colocalization of mRNA
631 transcripts with CRF+ (tdTomato) neurons, Scan 1 (pre-assay) and Scan 2 (post-assay)
632 images were aligned and merged using RNAscope HiPlex Image Registration Software
633 v2.1 (ACD). This process allowed for the simultaneous analysis of *vGlut2*, *vGat*, and
634 *Gad2* expression within the previously identified tdTomato-labeled CRF+ population.
635 **Image Analysis and RNAscope Quantification**
636 QuPath Identification and Annotation: Quantitative analysis of CRF+ (tdTomato+)
637 neurons and their co-expression of *Slc32a1* (vGAT), *Gad2* (GAD2), and *Slc17a6*
638 (vGLUT2) mRNA was performed using QuPath (v0.5.0) image analysis software. The
639 LHb was anatomically delineated in each section using the Allen Mouse Brain Atlas in
640 conjunction with the Paxinos and Franklin Mouse Brain Atlas as reference. The LHb
641 perimeter was manually outlined using the closed polygon annotation tool to create a
642 defined Region of Interest (ROI) for automated analysis.

643 Cell Detection and Phenotypic Classification: Individual CRF+ neurons were identified
644 and segmented within the LHb ROI using the Cell Detection tool, which utilized the
645 tdTomato fluorescence signal for primary cell identification. Following detection, cells
646 were systematically classified based on the presence of multiplexed RNAscope puncta.
647 Phenotypes were categorized as:

648 - Single-positive: vGLUT2+, vGAT+, or GAD2+
649 - Dual-positive: vGLUT2+/vGAT+, vGLUT2+/GAD2+, or vGAT+/GAD2+
650 - Triple-positive: vGLUT2+/vGAT+/GAD2+

651 Anatomical Sampling and Statistical Representation: Quantification was conducted on
652 coronal sections from CRH-Cre::Ai14 mice (n=13; 7 males, 6 females). To ensure an
653 unbiased longitudinal assessment, cells were quantified across five distinct anterior-
654 posterior (AP) levels of the LHb, ranging from Bregma -1.06 to -2.18mm.
655 Data are reported as the absolute number of CRF+ cells per section. Phenotypic
656 distributions (e.g., percentage of dual- or triple-positive neurons) were calculated as a
657 proportion of the total CRF+ population, noting that 100% of the identified CRF+
658 neurons were also positive for vGLUT2.
659

660 **Immunohistochemistry**

661 At least three weeks following viral injection, similar to RNAScope procedure, mice were
662 anesthetized and perfused transcardially and brain sections (20 μm) were cut using a
663 cryostat, generating a series from Bregma 2.10 to -5.68mm AP. Sections were mounted
664 on slides. For immunolabeling, LHb sections from CRH-Cre mice injected with rgAAV-
665 EF1a-DIO EYFP (for parvalbumin staining) or CRH-Cre:Ai14 mice injected with AAV8-

666 DIO-HA-hM3D(Gq)-mCitrine (for HA-tag staining) were blocked in 0.3% Triton X-100
667 containing 10% Normal Goat Serum (NGS) in 1x PBS for 1 hour and then incubated
668 overnight at room temperature in carrier solution (5% NGS in 0.1% Triton X-100 in 1x
669 PBS) with: mouse anti-parvalbumin IgG1 antibody (1:1000, Sigma, P3088) to detect
670 parvalbumin expression in retrogradely labeled LHb^{CRF} neurons or rabbit anti-human
671 influenza hemagglutinin (HA) antibody (1:500, Cell Signaling) to detect HA-hM3Dq in
672 tdTomato-expressing LHb neurons.
673 Sections were rinsed in 1x PBS and incubated for 2 hours in Alexa Fluor® 594-labeled
674 Goat anti-Mouse IgG1 or Alexa Fluor® 647-labeled Goat anti-Rabbit. Sections were
675 rinsed again in 1x PBS and coverslipped with Prolong Gold mounting medium
676 containing DAPI. Background staining was assessed by omitting the primary antibody
677 (negative control). Brain tissue sections with known parvalbumin immunoreactivity
678 (cortex, hippocampus) were also processed as positive control tissues. Images were
679 captured using a Leica DMRXA Fluorescence microscope.
680 **Anterograde Projection Mapping and Histological Imaging**
681 At least three weeks following viral injection, mice were anesthetized and underwent
682 transcardial perfusion with 4% PFA, following the same standardized protocol used for
683 RNAscope and immunohistochemistry. Brains were post-fixed, cryoprotected, and
684 subsequently sectioned at 20 μm using a cryostat. To ensure a comprehensive mapping
685 of projection targets, a continuous series of coronal sections was collected across the
686 rostrocaudal axis, spanning from Bregma +2.10 to -5.68 mm. To map the efferent
687 projection patterns of LHb^{CRF} neurons, three distinct anterograde viral strategies were
688 employed. In our primary approach (Figures 5–6), CRH-Cre::Ai6 mice of both sexes

689 were injected with AAV5-Syn-FLEX-ChrimsonR-tdTomato. For automated histological
690 imaging, sections were scanned using a Zeiss Axioscan equipped with a 20x objective.
691 This configuration permitted the simultaneous capture of the endogenous GFP (green)
692 signal—representing the global population of CRF+ neurons via the Ai6 reporter—and
693 the tdTomato (red) signal, marking the specific axonal projections originating from
694 ChrimsonR-expressing CRF+ neurons in the LHb. The resulting high-resolution mosaic
695 images were utilized to verify injection site specificity and to trace efferent fibers across
696 multiple neuroanatomical targets along the rostrocaudal axis. Two alternative strategies
697 were initially used to map these projections: AAV8-hSyn-DIO-mCherry injections in
698 male CRH-Cre mice and AAV5-Ef1a-DIO-ChR2-EYFP injections in female CRH-Cre
699 mice. While these initial experiments identified consistent projections to the LHb, RMTg,
700 SNc, and PAG, we subsequently transitioned to the ChrimsonR-tdTomato approach in
701 the Ai6 reporter line. This refined strategy allowed for a more rigorous, sex-balanced
702 comparison and, when combined with the Zeiss Axioscan, provided superior sensitivity
703 in detecting additional efferent projections. Consequently, the results from the initial
704 ChR2 and mCherry experiments were documented as supplementary data
705 (Supplementary Figures 8 and 9), with images captured using a Leica DMRXA
706 fluorescence microscope.

707 **Quantification of Retrogradely Labeled CRF+ Neurons**

708 To quantify the regional distribution of LHb-projecting CRF+ neurons, EYFP-labeled cell
709 bodies were identified and mapped using the Allen Mouse Brain Atlas in conjunction
710 with the Paxinos and Franklin Mouse Brain Atlas. Analysis was conducted on coronal
711 sections from three CRH-Cre mice (n = 3; 2 males, 1 female). The total number of

712 retrogradely labeled neurons analyzed per subject was 2,211 (CRH-Cre 1), 3,309
713 (CRH-Cre 2), and 1,750 (CRH-Cre 3). To ensure representative sampling across the
714 rostrocaudal axis, labeled cells were counted within defined regions of interest (ROIs)
715 across three consecutive sections (inter-section interval of 0.12 mm). Data are
716 expressed as a percentage of the total population of labeled neurons identified across
717 all ROIs:
718 Percentage of Labeled Neurons = (Cells in ROI / Total Labeled Cells) X 100
719 Forebrain and hypothalamic ROIs included the bed nucleus of the stria terminalis
720 (BNST; Bregma +0.14 to -0.22 mm), lateral preoptic area (LPO; Bregma +0.38 to -0.22
721 mm), paraventricular hypothalamic nucleus (PVH; Bregma -0.34 to -1.46 mm), and
722 lateral hypothalamus (LHA; Bregma -0.34 to -1.34 mm). Midbrain and thalamic targets
723 sampled included the paraventricular thalamic nucleus (PVT; Bregma -1.34 to -2.30
724 mm), lateral habenula (LHb; Bregma -1.06 to -2.30 mm), and posterior hypothalamus
725 (PH; Bregma -2.06 to -2.80 mm). Posterior midbrain and brainstem structures included
726 the pretectal area (PRT, including the medial pretectal nucleus; Bregma -2.46 to -2.80
727 mm), midbrain reticular nucleus (MRN; Bregma -2.54 to -3.80 mm), superior colliculus
728 (SC; Bregma -2.80 to -3.92 mm), and the periaqueductal gray (PAG; Bregma -2.30 to -
729 4.04 mm). Figure 1 and supplementary Figure 1 include the data derived from this
730 experiment.

731 **Ex Vivo Slice Electrophysiology and Optogenetics**

732 **Slice Preparation**

733 Electrophysiology experiments were conducted using male and female CRH-Cre::Ai14
734 reporter mice or CRH-Cre::Ai6 mice. For optogenetic experiments, CRH-Cre::Ai6 mice

735 were previously injected with a Cre-dependent anterograde vector (AAV5-Syn-FLEX-
736 ChrimsonR-tdTomato) into the LHb. To allow for robust opsin expression and trafficking
737 to distal terminals, all physiological recordings were performed at a minimum of three
738 weeks post-injection. Mice were deeply anesthetized with isoflurane and decapitated.
739 Brains were rapidly dissected and placed in ice-cold artificial cerebrospinal fluid (ACSF)
740 containing (in mM): 126 NaCl, 21.4 NaHCO3, 2.5 KCl, 1.2 NaH2PO4, 2.4 CaCl2, 1.00
741 MgSO4, 11.1 glucose, 0.4 ascorbic acid; saturated with 95% O2-5% CO2.
742 Sagittal or coronal slices (220μm) containing the LHb were cut using a vibratome (Leica;
743 Wetzlar, Germany) and incubated in oxygenated ACSF at 34°C for at least 1 hour prior
744 to recording. For all experiments, slices were transferred to a recording chamber and
745 perfused with ascorbic-acid-free ACSF maintained at 28–30°C.

746 **General Recording Conditions**

747 Whole-cell patch-clamp recordings were performed using an upright microscope
748 (Olympus BX51WI) equipped with infrared-differential interference contrast (IR-DIC)
749 microscopy. Patch pipettes (3–6 MΩ) were controlled via a MultiClamp 700B amplifier,
750 digitized with a DigiData 1440A, and analyzed using pCLAMP 10 (Molecular Devices)
751 and GraphPad Prism 10. Signals were filtered at 3kHz and digitized at 10kHz. Input and
752 series resistances were monitored throughout; data were excluded if these values
753 fluctuated by more than 10%.

754 **Intrinsic Excitability and Firing Patterns**

755 To assess intrinsic properties of LHb^{CRF} neurons in male and female CRH-Cre::Ai14
756 mice, pipettes were filled with a potassium gluconate-based internal solution (130 mM
757 K-gluconate, 15 mM KCl, 4 mM ATP-Na+, 0.3 mM GTP-Na+, 1 mM EGTA, and 5 mM

758 HEPES, pH adjusted to 7.28 with KOH, osmolarity adjusted to 275-280 mOsm).
759 Spontaneous neuronal activity and action potential (AP) firing patterns (e.g., tonic vs.
760 bursting) were recorded in cell-attached voltage-clamp mode (V = 0) for approximately
761 one minute. To assess excitability, neurons were maintained at -65 to -70mV via
762 manual DC injection. Increasingly depolarizing current steps (5s duration) were applied
763 at +10pA intervals (ranging from +10 to +100pA) with a 20s inter-stimulus interval. The
764 number of APs generated per step was quantified and averaged by experimental group.

765 **Optogenetic dissection of local LHb^{CRF} connectivity**

766 To investigate local synaptic connections, recordings were obtained from non-CRF LHb
767 neurons (GFP-negative) while optogenetically stimulating local CRF+ terminals within
768 the LHb in male and female CRH-Cre::Ai6 mice (injected with AAV5-Syn-FLEX-
769 ChrimsonR-tdTomato). For these experiments, pipettes were filled with a cesium
770 gluconate-based internal solution (117 mM CsGlc, 2.8 mM NaCl, 5 mM $MgCl_2$, 2 mM
771 ATP-Na+, 0.3 mM GTP-Na+, 0.6 mM EGTA, and 20 mM HEPES, pH 7.28, osmolality
772 275–280 mOsm). Optogenetic stimulation (590nm LED; X-Cite XLED1, Lumen
773 Dynamics) was delivered through a 40x0.8NA objective of an upright microscope
774 (Olympus, BX51WI). Light pulses (1ms) were delivered at intensities of 0.1-
775 1.0mW/mm^2. To determine the input/output (I/O) relationship of the local synapses, peak
776 AMPAR-mediated oEPSCs were recorded at a holding potential of -70mV across increasing
777 LED intensity levels (0–100%). To control for variations in viral expression levels, data were
778 then normalized for each neuron and expressed as a percentage of the minimum and maximal
779 amplitude responses recorded across the intensity range.
780 Neurons were also held at specific potentials to further characterize synaptic inputs:

781 - +10mV: To confirm the absence of inhibitory currents (oIPSCs) at the glutamate
782 reversal potential.
783 - +40mV: To evoke mixed AMPA- and NMDA-mediated oEPSCs.

784 The NMDAR-mediated component was isolated at +40mV by measuring current
785 amplitude 20ms post-AMPAR peak (~50ms post-LED trigger). For paired-pulse ratio
786 (PPR) experiments, two light pulses were delivered with a 100ms inter-pulse interval
787 and a 20s inter-trial interval. Peak amplitudes for both evoked oEPSCs (P1 and P2)
788 were measured relative to a stable baseline, which was defined as the average current
789 during a 20–50ms window immediately preceding the first light-evoked current. The
790 PPR was calculated as the ratio of the peak amplitude of the second response to the
791 first (P2/P1) at each intensity level.

792 **Pharmacological Validation**

793 To confirm monosynaptic, glutamatergic transmission, a subset of experiments utilized
794 bath application of the sodium channel blocker tetrodotoxin (TTX, 1μM), followed by the
795 potassium channel blocker 4-aminopyridine (4-AP, 50μM) to rescue monosynaptic
796 oEPSCs.

797 **Behavioral assays with chemogenetics**

798 Four weeks post-viral injections, behavioral testing began with separate cohorts of
799 CRH-Cre or CRH-Cre::Ai14 male and female mice expressing Gq DREADD in LHb.
800 Mice received intraperitoneal injections of either 0.3mg/kg of the DREADD ligand,
801 JHU37160, or vehicle (equivalent volumes of 0.9% saline) 30 min prior to behavioral
802 testing, consistent with our previous study[55]. In the CPP test, DREADD-injected mice
803 underwent conditioning with JHU37160 paired with either the preferred or non-preferred

804 side of the chamber in a balanced (unbiased) manner. In these cohorts, JHU37160 or
805 saline was administered only during conditioning days (days 2-3), not during habituation
806 (day 1) or testing (day 4).

807 **Open field test (OFT)**

808 Mice were placed in an open field arena (40 cm x 40 cm) with dim white lighting (~5lux)
809 and allowed to explore freely for 15 minutes. Animal movement was tracked using Any-
810 Maze video tracking software (Stoelting Co.), recording distance traveled and time
811 spent in the periphery and center zones.

812 **Elevated zero maze (EZM)**

813 To assess anxiety and risk-taking behavior, mice were placed in an elevated zero maze
814 and allowed to freely explore for 10 minutes with dim white lighting (~5lux). The maze,
815 elevated 40 cm above the floor, comprises a ring-shaped arena with four arms (5 cm x
816 30 cm): two enclosed arms with 20-cm high walls and two open arms. An overhead
817 camera and Any-Maze software (Stoelting Co.) were used to track the animal's
818 movement, quantifying the number of entries and the time spent in both the open and
819 closed arms, along with the total distance traveled.

820 **Light-Dark Test (LDT)**

821 The light-dark box test, similar in concept to the elevated zero maze but without the
822 height factor, consists of a 40 cm x 40 cm box divided into a dark, enclosed chamber
823 and a bright, exposed chamber (~750lux). While mice prefer the dark chamber, they
824 also explore the bright area. Less time spent in the light chamber and more time in the
825 dark is interpreted as higher anxiety. An overhead camera and Any-Maze software

826 (Stoelting Co.) tracked the animal's position, recording distance traveled and time spent
827 in each chamber.

828 **Conditioned place preference (CPP)**

829 We employed a three-compartment apparatus to conduct CPP testing. This apparatus
830 featured outer compartments with distinct visual cues (e.g., circles vs. triangles walls)
831 and a small central compartment lacking specific cues. Gates allowed mice to freely
832 traverse the three compartments. Anymaze software was used to track the time spent in
833 each compartment during the pre-test, conditioning, and test phases. The CPP
834 procedure comprised: Pretest (Day 1): To assess baseline preferences, each mouse
835 was placed in the central compartment and allowed to explore all three compartments
836 for 20 minutes. Conditioning (Days 2-3): Mice underwent conditioning sessions wherein
837 they were confined to one outer compartment and administered saline, followed by
838 confinement to the opposite compartment (after a >4-hour interval) and administration of
839 either saline or JHU37160 (30 minutes prior to confinement). The pairing of saline or
840 JHU37160 with a specific compartment was balanced across animals. Test (Day 4):
841 Mice were given free access to all compartments, and the time spent in the
842 saline/JHU37160-paired compartment was measured to determine place preference.
843 Place preference was quantified by calculating a preference score: time spent in the
844 saline/JHU37160-paired compartment during the post-test minus time spent in that
845 compartment during the pre-test (post-pre).

846 **Looming-shadow test**

847 This test simulates a predator threat to induce defensive behaviors in mice, which
848 manifest as either passive action-locking/freezing or active escape. The testing

environment consisted of a 17 x 10 x 8.5-inch plastic arena with a 21-inch LCD monitor positioned overhead to present the visual stimulus. A 6 x 6 x 3-inch shelter was placed on one side of the arena. Behavior was recorded with a camera positioned laterally above the arena. First, mice were habituated to the arena for two days (10 minutes/day). On the test day, there was a 5-minute habituation period within the arena before stimulus presentation and then mice were presented with five looming visual stimuli, with at least a 1-minute inter-trial interval. The stimulus comprised of a 2-cm black disk expanding to 20 cm over 9 seconds, divided into three phases: 2 seconds at 2 cm, 5 seconds of expansion, and 2 seconds at 20 cm. Defensive responses were classified as: escape (active movement to the shelter), action-locking/freezing (absence of movement or repeated, discontinuous freezing) and action-locking to escape behavior (action-locking that transitions to escape in which mice exhibit an immediate freezing behavior followed by a delayed escape to the shelter). Mice were excluded as non-responders if they exhibited no discernible reaction to the looming stimulus (no freezing, no behavioral change, and failure to reach the shelter within 8 seconds). Video recordings were used to blindly score the type of defensive behavior and the latency to escape. For each subject, escape latencies, shelter stay, and action locking duration were averaged across the five looming trials; these mean values were then used for all subsequent statistical analyses and are presented as individual data points.

Statistics and reproducibility

Data are presented as mean ± SEM. Statistical significance was assessed using unpaired two-tailed Student's t-tests, Chi-square tests, and two-way ANOVA with

871 Bonferroni post hoc tests. A significance threshold of $P < 0.05$ was used for all
872 analyses. Statistical analyses were performed using GraphPad Prism 10.

873 **Data availability**

874 Data supporting the conclusions of this study are available from the corresponding
875 author upon reasonable request.

876 **References**

877 1 Hu, H., Cui, Y. & Yang, Y. Circuits and functions of the lateral habenula in health and in disease.
878 *Nat Rev Neurosci* **21**, 277–295 (2020). https://doi.org/10.1038/s41583-020-0292-4
879 2 Groos, D. & Helmchen, F. The lateral habenula: A hub for value-guided behavior. *Cell reports* **43**,
880 113968 (2024). https://doi.org/https://doi.org/10.1016/j.celrep.2024.113968
881 3 Baker, P. M. *et al.* Lateral Habenula Beyond Avoidance: Roles in Stress, Memory, and Decision-
882 Making With Implications for Psychiatric Disorders. *Front Syst Neurosci* **16**, 826475 (2022).
883 https://doi.org/10.3389/fnsys.2022.826475
884 4 Proulx, C. D., Hikosaka, O. & Malinow, R. Reward processing by the lateral habenula in normal
885 and depressive behaviors. *Nature neuroscience* **17**, 1146–1152 (2014).
886 https://doi.org/10.1038/nn.3779
887 5 Wang, D. *et al.* Learning shapes the aversion and reward responses of lateral habenula neurons.
888 *eLife* **6**, e23045 (2017). https://doi.org/10.7554/eLife.23045
889 6 Hashikawa, Y. *et al.* Transcriptional and Spatial Resolution of Cell Types in the Mammalian
890 Habenula. *Neuron* **106**, 743–758 e745 (2020). https://doi.org/10.1016/j.neuron.2020.03.011
891 7 Nguyen, T. V. T., Nakamura, T. & Ichijo, H. Topographic Organization of Glutamatergic and
892 GABAergic Parvalbumin-Positive Neurons in the Lateral Habenula. *eNeuro* **11** (2024).
893 https://doi.org/10.1523/ENEURO.0069-24.2024
894 8 Flanigan, M. E. *et al.* Orexin signaling in GABAergic lateral habenula neurons modulates
895 aggressive behavior in male mice. *Nature neuroscience* **23**, 638–650 (2020).
896 https://doi.org/10.1038/s41593-020-0617-7
897 9 Zhang, L. *et al.* A GABAergic cell type in the lateral habenula links hypothalamic homeostatic and
898 midbrain motivation circuits with sex steroid signaling. *Translational psychiatry* **8**, 50 (2018).
899 https://doi.org/10.1038/s41398-018-0099-5
900 10 Webster, J. F., Lecca, S. & Wozny, C. Inhibition Within the Lateral Habenula-Implications for
901 Affective Disorders. *Front Behav Neurosci* **15**, 786011 (2021).
902 https://doi.org/10.3389/fnbeh.2021.786011
903 11 Webster, J. F. *et al.* Disentangling neuronal inhibition and inhibitory pathways in the lateral
904 habenula. *Sci Rep* **10**, 8490 (2020). https://doi.org/10.1038/s41598-020-65349-7
905 12 Quina, L. A. *et al.* Efferent Pathways of the Mouse Lateral Habenula. *Journal of Comparative*
906 *Neurology* **523**, 32–60 (2015). https://doi.org/https://doi.org/10.1002/cne.23662
907 13 Zahm, D. S. & Root, D. H. Review of the cytology and connections of the lateral habenula, an
908 avatar of adaptive behaving. *Pharmacology, biochemistry, and behavior* **162**, 3–21 (2017).
909 https://doi.org/10.1016/j.pbb.2017.06.004
910 14 Hong, S., Jhou, T. C., Smith, M., Saleem, K. S. & Hikosaka, O. Negative reward signals from the
911 lateral habenula to dopamine neurons are mediated by rostromedial tegmental nucleus in

primates. *J Neurosci* **31**, 11457–11471 (2011). https://doi.org/10.1523/JNEUROSCI.1384-11.2011

15 Mathis, V. P., Williams, M., Fillinger, C. & Kenny, P. J. Networks of habenula-projecting cortical neurons regulate cocaine seeking. *Science Advances* **7**, eabj2225 (2021). https://doi.org/doi:10.1126/sciadv.abj2225

16 Flerlage, W. J. *et al.* Dysregulation of kappa opioid receptor neuromodulation of lateral habenula synaptic function following a repetitive mild traumatic brain injury. *Pharmacology Biochemistry and Behavior* **243**, 173838 (2024). https://doi.org/https://doi.org/10.1016/j.pbb.2024.173838

17 Wallace, M. L. *et al.* Genetically Distinct Parallel Pathways in the Entopeduncular Nucleus for Limbic and Sensorimotor Output of the Basal Ganglia. *Neuron* **94**, 138–152 e135 (2017). https://doi.org/10.1016/j.neuron.2017.03.017

18 Li, H., Pullmann, D. & Jhou, T. C. Valence-encoding in the lateral habenula arises from the entopeduncular region. *Elife* **8** (2019). https://doi.org/10.7554/eLife.41223

19 Liu, B., Cao, Y., Wang, J. & Dong, J. Excitatory transmission from ventral pallidum to lateral habenula mediates depression. *World J Biol Psychiatry* **21**, 627–633 (2020). https://doi.org/10.1080/15622975.2020.1725117

20 Lecca, S. *et al.* Aversive stimuli drive hypothalamus-to-habenula excitation to promote escape behavior. *Elife* **6** (2017). https://doi.org/10.7554/eLife.30697

21 Liu, X., Huang, H., Zhang, Y., Wang, L. & Wang, F. Sexual Dimorphism of Inputs to the Lateral Habenula in Mice. *Neuroscience bulletin* **38**, 1439–1456 (2022). https://doi.org/10.1007/s12264-022-00885-y

22 Golden, S. A. *et al.* Basal forebrain projections to the lateral habenula modulate aggression reward. *Nature* **534**, 688–692 (2016). https://doi.org/10.1038/nature18601

23 Zhang, G. W. *et al.* Transforming Sensory Cues into Aversive Emotion via Septal-Habenular Pathway. *Neuron* **99**, 1016–1028.e1015 (2018). https://doi.org/10.1016/j.neuron.2018.07.023

24 Root, D. H. *et al.* Single rodent mesohabenular axons release glutamate and GABA. *Nature neuroscience* **17**, 1543–1551 (2014). https://doi.org/10.1038/nn.3823

25 Lima, L. B. *et al.* Afferent and efferent connections of the interpeduncular nucleus with special reference to circuits involving the habenula and raphe nuclei. *The Journal of comparative neurology* **525**, 2411–2442 (2017). https://doi.org/10.1002/cne.24217

26 Hwang, E. K. *et al.* Basal forebrain-lateral habenula inputs and control of impulsive behavior. *Neuropsychopharmacology* **49**, 2060–2068 (2024). https://doi.org/10.1038/s41386-024-01963-7

27 Wolfe, C. I. C. *et al.* Muscarinic Acetylcholine M₂ Receptors Regulate Lateral Habenula Neuron Activity and Control Cocaine Seeking Behavior. *The Journal of Neuroscience* **42**, 5552–5563 (2022). https://doi.org/10.1523/jneurosci.0645-22.2022

28 Fu, R. *et al.* Anxiety during alcohol withdrawal involves 5-HT2C receptors and M-channels in the lateral habenula. *Neuropharmacology* **163**, 107863 (2020). https://doi.org/10.1016/j.neuropharm.2019.107863

29 Zuo, W. *et al.* Serotonin stimulates lateral habenula via activation of the post-synaptic serotonin 2/3 receptors and transient receptor potential channels. *Neuropharmacology* **101**, 449–459 (2016). https://doi.org/10.1016/j.neuropharm.2015.10.012

30 Shabel, S. J., Proulx, C. D., Trias, A., Murphy, R. T. & Malinow, R. Input to the lateral habenula from the Basal Ganglia is excitatory, aversive, and suppressed by serotonin. *Neuron* **74**, 475–481 (2012). https://doi.org/10.1016/j.neuron.2012.02.037

31 Root, D. H. *et al.* Norepinephrine activates dopamine D4 receptors in the rat lateral habenula. *J Neurosci* **35**, 3460–3469 (2015). https://doi.org/10.1523/JNEUROSCI.4525-13.2015

958 32 Cheon, M., Park, H. & Chung, C. Protein kinase C mediates neuropeptide Y-induced reduction in
959 inhibitory neurotransmission in the lateral habenula. *Neuropharmacology* **180**, 108295 (2020).
960 https://doi.org/https://doi.org/10.1016/j.neuropharm.2020.108295
961 33 Cheon, M., Park, H., Rhim, H. & Chung, C. Actions of Neuropeptide Y on Synaptic Transmission in
962 the Lateral Habenula. *Neuroscience* **410**, 183–190 (2019).
963 https://doi.org/10.1016/j.neuroscience.2019.04.053
964 34 Simmons, S. C. *et al.* Early life stress dysregulates kappa opioid receptor signaling within the
965 lateral habenula. *Neurobiol Stress* **13**, 100267 (2020).
966 https://doi.org/10.1016/j.ynstr.2020.100267
967 35 Simmons, S. C. *et al.* AKAP150-anchored PKA regulates synaptic transmission and plasticity,
968 neuronal excitability and CRF neuromodulation in the mouse lateral habenula. *Communications*
969 *Biology* **7**, 345 (2024). https://doi.org/10.1038/s42003-024-06041-8
970 36 Flerlage, W. J. *et al.* Effects of Repetitive Mild Traumatic Brain Injury on Corticotropin-Releasing
971 Factor Modulation of Lateral Habenula Excitability and Motivated Behavior. *J Neurotrauma*
972 (2024). https://doi.org/10.1089/neu.2024.0184
973 37 Zuo, W. *et al.* Roles of corticotropin-releasing factor signaling in the lateral habenula in anxiety-
974 like and alcohol drinking behaviors in male rats. *Neurobiol Stress* **15**, 100395 (2021).
975 https://doi.org/10.1016/j.ynstr.2021.100395
976 38 Authement, M. E. *et al.* A role for corticotropin-releasing factor signaling in the lateral habenula
977 and its modulation by early-life stress. *Science signaling* **11** (2018).
978 https://doi.org/10.1126/scisignal.aan6480
979 39 Henckens, M. J., Deussing, J. M. & Chen, A. Region-specific roles of the corticotropin-releasing
980 factor-urocortin system in stress. *Nat Rev Neurosci* **17**, 636–651 (2016).
981 https://doi.org/10.1038/nrn.2016.94
982 40 Bangasser, D. A. & Wiersielis, K. R. Sex differences in stress responses: a critical role for
983 corticotropin-releasing factor. *Hormones* **17**, 5–13 (2018). https://doi.org/10.1007/s42000-018-
984 0002-z
985 41 Levinstein, M. R. *et al.* PACAP-expressing neurons in the lateral habenula diminish negative
986 emotional valence. *Genes Brain Behav*, e12801 (2022). https://doi.org/10.1111/gbb.12801
987 42 Sandoval, K. C., Rychlik, J. & Choe, K. Y. Calcium Dynamics in Hypothalamic Paraventricular
988 Oxytocin Neurons and Astrocytes Associated with Social and Stress Stimuli. *eNeuro* **12** (2025).
989 https://doi.org/10.1523/ENEURO.0196-24.2025
990 43 Daviu, N. *et al.* Paraventricular nucleus CRH neurons encode stress controllability and regulate
991 defensive behavior selection. *Nature neuroscience* **23**, 398–410 (2020).
992 https://doi.org/10.1038/s41593-020-0591-0
993 44 Lecca, S. *et al.* Heterogeneous Habenular Neuronal Ensembles during Selection of Defensive
994 Behaviors. *Cell reports* **31**, 107752 (2020). https://doi.org/10.1016/j.celrep.2020.107752
995 45 Rasiah, N. *et al.* Homeostatic scaling ensures behavioural stability during corticosterone negative
996 feedback. *Molecular psychiatry* (2025). https://doi.org/10.1038/s41380-025-03391-5
997 46 Madisen, L. *et al.* A robust and high-throughput Cre reporting and characterization system for
998 the whole mouse brain. *Nature neuroscience* **13**, 133–140 (2010).
999 https://doi.org/10.1038/nn.2467
1000 47 Madisen, L. *et al.* Transgenic mice for intersectional targeting of neural sensors and effectors
1001 with high specificity and performance. *Neuron* **85**, 942–958 (2015).
1002 https://doi.org/10.1016/j.neuron.2015.02.022
1003 48 Chen, Y., Molet, J., Gunn, B. G., Ressler, K. & Baram, T. Z. Diversity of Reporter Expression
1004 Patterns in Transgenic Mouse Lines Targeting Corticotropin-Releasing Hormone-Expressing
1005 Neurons. *Endocrinology* **156**, 4769–4780 (2015). https://doi.org/10.1210/en.2015-1673

1006 49 Füzesi, T., Daviu, N., Wamsteeker Cusulin, J. I., Bonin, R. P. & Bains, J. S. Hypothalamic CRH
1007 neurons orchestrate complex behaviours after stress. *Nature communications* **7**, 11937 (2016).
1008 https://doi.org/10.1038/ncomms11937
1009 50 Birnie, M. T. *et al.* Stress-induced plasticity of a CRH/GABA projection disrupts reward behaviors
1010 in mice. *Nature communications* **14**, 1088 (2023). https://doi.org/10.1038/s41467-023-36780-x
1011 51 Paretkar, T. & Dimitrov, E. The Central Amygdala Corticotropin-releasing hormone (CRH)
1012 Neurons Modulation of Anxiety-like Behavior and Hippocampus-dependent Memory in Mice.
1013 *Neuroscience* **390**, 187–197 (2018). https://doi.org/10.1016/j.neuroscience.2018.08.019
1014 52 Birnie, M. T. *et al.* Stress-induced plasticity of a CRH/GABA projection disrupts reward behaviors
1015 in mice. *Nature communications* **14**, 1088 (2023). https://doi.org/10.1038/s41467-023-36780-x
1016 53 Lin, J. Y., Knutsen, P. M., Muller, A., Kleinfeld, D. & Tsien, R. Y. ReaChR: a red-shifted variant of
1017 channelrhodopsin enables deep transcranial optogenetic excitation. *Nature neuroscience* **16**,
1018 1499–1508 (2013). https://doi.org/10.1038/nn.3502
1019 54 Goyer, D. & Roberts, M. T. Long-range Channelrhodopsin-assisted Circuit Mapping of Inferior
1020 Colliculus Neurons with Blue and Red-shifted Channelrhodopsins. *J Vis Exp* (2020).
1021 https://doi.org/10.3791/60760
1022 55 Flerlage, W. J. *et al.* Involvement of Lateral Habenula Dysfunction in Repetitive Mild Traumatic
1023 Brain Injury-Induced Motivational Deficits. *J Neurotrauma* **40**, 125–140 (2023).
1024 https://doi.org/10.1089/neu.2022.0224
1025 56 Lawson, R. P. *et al.* Disrupted habenula function in major depression. *Molecular psychiatry* **22**,
1026 202–208 (2017). https://doi.org/10.1038/mp.2016.81
1027 57 Weidacker, K. *et al.* Avoiding monetary loss: A human habenula functional MRI ultra-high field
1028 study. *Cortex* **142**, 62–73 (2021). https://doi.org/https://doi.org/10.1016/j.cortex.2021.05.013
1029 58 Abraham, M. E. *et al.* Investigating Deep Brain Stimulation of the Habenula: A Review of Clinical
1030 Studies. *Neuromodulation: Technology at the Neural Interface* **26**, 292–301 (2023).
1031 https://doi.org/https://doi.org/10.1016/j.neurom.2022.05.005
1032 59 Samanci, B., Tan, S., Michielse, S., Kuijf, M. L. & Temel, Y. The habenula in Parkinson's disease:
1033 Anatomy, function, and implications for mood disorders − A narrative review. *Journal of*
1034 *chemical neuroanatomy* **136**, 102392 (2024).
1035 https://doi.org/https://doi.org/10.1016/j.jchemneu.2024.102392
1036 60 Proulx, C. D., Hikosaka, O. & Malinow, R. Reward processing by the lateral habenula in normal
1037 and depressive behaviors. *Nature neuroscience* **17**, 1146–1152 (2014).
1038 https://doi.org/10.1038/nn.3779
1039 61 Arfuso, M., Salas, R., Castellanos, F. X. & Krain Roy, A. Evidence of Altered Habenular Intrinsic
1040 Functional Connectivity in Pediatric ADHD. *J Atten Disord* **25**, 749–757 (2021).
1041 https://doi.org/10.1177/1087054719843177
1042 62 Lee, Y.-A. & Goto, Y. The Habenula in the Link Between ADHD and Mood Disorder. *Frontiers in*
1043 *Behavioral Neuroscience* **15** (2021). https://doi.org/10.3389/fnbeh.2021.699691
1044 63 Lawson, R. P., Drevets, W. C. & Roiser, J. P. Defining the habenula in human neuroimaging
1045 studies. *NeuroImage* **64**, 722–727 (2013).
1046 https://doi.org/https://doi.org/10.1016/j.neuroimage.2012.08.076
1047 64 Zhu, Y. *et al.* Connectome-Based Biomarkers Predict Subclinical Depression and Identify
1048 Abnormal Brain Connections With the Lateral Habenula and Thalamus. *Frontiers in psychiatry* **10**
1049 (2019). https://doi.org/10.3389/fpsyt.2019.00371
1050 65 Wallace, M. L. *et al.* Anatomical and single-cell transcriptional profiling of the murine habenular
1051 complex. *Elife* **9** (2020). https://doi.org/10.7554/eLife.51271

66 Cerniauskas, I. *et al.* Chronic Stress Induces Activity, Synaptic, and Transcriptional Remodeling of the Lateral Habenula Associated with Deficits in Motivated Behaviors. *Neuron* **104**, 899–915 e898 (2019). https://doi.org/10.1016/j.neuron.2019.09.005

67 Zhang, L., Hernandez, V. S., Vazquez-Juarez, E., Chay, F. K. & Barrio, R. A. Thirst Is Associated with Suppression of Habenula Output and Active Stress Coping: Is there a Role for a Non-canonical Vasopressin-Glutamate Pathway? *Frontiers in neural circuits* **10**, 13 (2016). https://doi.org/10.3389/fncir.2016.00013

68 Margolis, E. B. & Fields, H. L. Mu Opioid Receptor Actions in the Lateral Habenula. *PLoS One* **11**, e0159097 (2016). https://doi.org/10.1371/journal.pone.0159097

69 Cui, J., Qian, J., Wang, J. & Shi, L. Decoding the dual regulatory systems: Contemporary insights into the lateral habenula and rostromedial tegmental nucleus physiology. *Neurobiology of Disease* **214**, 107049 (2025). https://doi.org/https://doi.org/10.1016/j.nbd.2025.107049

70 Huang, H., Liu, X., Wang, L. & Wang, F. Whole-brain connections of glutamatergic neurons in the mouse lateral habenula in both sexes. *Biology of Sex Differences* **15**, 37 (2024). https://doi.org/10.1186/s13293-024-00611-5

71 Quina, L. A., Walker, A., Morton, G., Han, V. & Turner, E. E. GAD2 Expression Defines a Class of Excitatory Lateral Habenula Neurons in Mice that Project to the Raphe and Pontine Tegmentum. *eNeuro* **7** (2020). https://doi.org/10.1523/eneuro.0527-19.2020

72 Quina, L. A. *et al.* Efferent pathways of the mouse lateral habenula. *The Journal of comparative neurology* **523**, 32–60 (2015). https://doi.org/10.1002/cne.23662

73 Chudoba, R. & Dabrowska, J. Distinct populations of corticotropin-releasing factor (CRF) neurons mediate divergent yet complementary defensive behaviors in response to a threat. *Neuropharmacology* **228**, 109461 (2023). https://doi.org/10.1016/j.neuropharm.2023.109461

74 Bastos, A. F. *et al.* Stop or move: Defensive strategies in humans. *Behavioural brain research* **302**, 252–262 (2016). https://doi.org/https://doi.org/10.1016/j.bbr.2016.01.043

75 Sippel, L. M., Taverna, E. & Marshall, A. D. In vivo defensive behaviors, fear, and attention bias to physical and negative evaluation threats. *Behaviour Research and Therapy* **154**, 104108 (2022). https://doi.org/https://doi.org/10.1016/j.brat.2022.104108

76 Roelofs, K., Hagenaars, M. A. & Stins, J. Facing Freeze: Social Threat Induces Bodily Freeze in Humans. *Psychological Science* **21**, 1575–1581 (2010). https://doi.org/10.1177/0956797610384746

77 Roelofs, K. Freeze for action: neurobiological mechanisms in animal and human freezing. *Philosophical transactions of the Royal Society of London* **372** (2017). https://doi.org/10.1098/rstb.2016.0206

78 Kearney, B. E. & Lanius, R. A. The brain-body disconnect: A somatic sensory basis for trauma-related disorders. *Frontiers in neuroscience* **16**, 1015749 (2022). https://doi.org/10.3389/fnins.2022.1015749

79 Sege, C. T., Bradley, M. M. & Lang, P. J. Avoidance and escape: Defensive reactivity and trait anxiety. *Behav Res Ther* **104**, 62–68 (2018). https://doi.org/10.1016/j.brat.2018.03.002

80 Baumgartner, H. M., Schulkin, J. & Berridge, K. C. Activating Corticotropin-Releasing Factor Systems in the Nucleus Accumbens, Amygdala, and Bed Nucleus of Stria Terminalis: Incentive Motivation or Aversive Motivation? *Biological psychiatry* **89**, 1162–1175 (2021). https://doi.org/10.1016/j.biopsych.2021.01.007

1096 **Acknowledgements:** The opinions and assertions contained herein are the private
1097 opinions of the authors and are not to be construed as official or reflecting the views of
1098 the Uniformed Services University of the Health Sciences or the Department of Defense
1099 or the Government of the United States. This work was supported by the National
1100 Institute of Mental Health (NIH/NIMH) Grant# R21 MH132136 to FSN. The funding
1101 agency did not contribute to writing this article or deciding to submit it. We gratefully
1102 acknowledge the Preclinical Behavior and Modeling Core for providing access to and
1103 support with their behavioral equipment, which was essential for the successful
1104 completion of this study.
1105 **Author contributions:** FSN and WJF designed the study. WJF, SCS, and EHT
1106 performed electrophysiology. TJW, SCG, and EHT were responsible for breeding CRH-
1107 Cre::Ai14 and CRH-Cre::Ai6 mice. SCG performed microscopy, RNAscope and
1108 immunohistochemistry, with assistance from LI and EP for RNAscope optimization.
1109 SCG, SCS, and WJF conducted viral stereotaxic injections. WJF, EHT, MCT, and SCS
1110 carried out chemogenetic behavioral assays. CMD assisted in analysis and
1111 interpretation of behavioral data. Data analysis and figure preparation were performed
1112 by WJF, SCG, SCS, EHT, OLR, and FSN. The initial manuscript draft was written by
1113 WJF, SCG, EHT, RCA, CMD, EP, BMC, and FSN. All authors critically reviewed and
1114 approved the final version of the manuscript.
1115 **Competing interests:** The authors declare no conflict of interest. Fereshteh Nugent is
1116 an Editorial Board Member for *Communications Biology*, but was not involved in the
1117 editorial review of, nor the decision to publish this article.
1118

1119 **Figure Legends:**

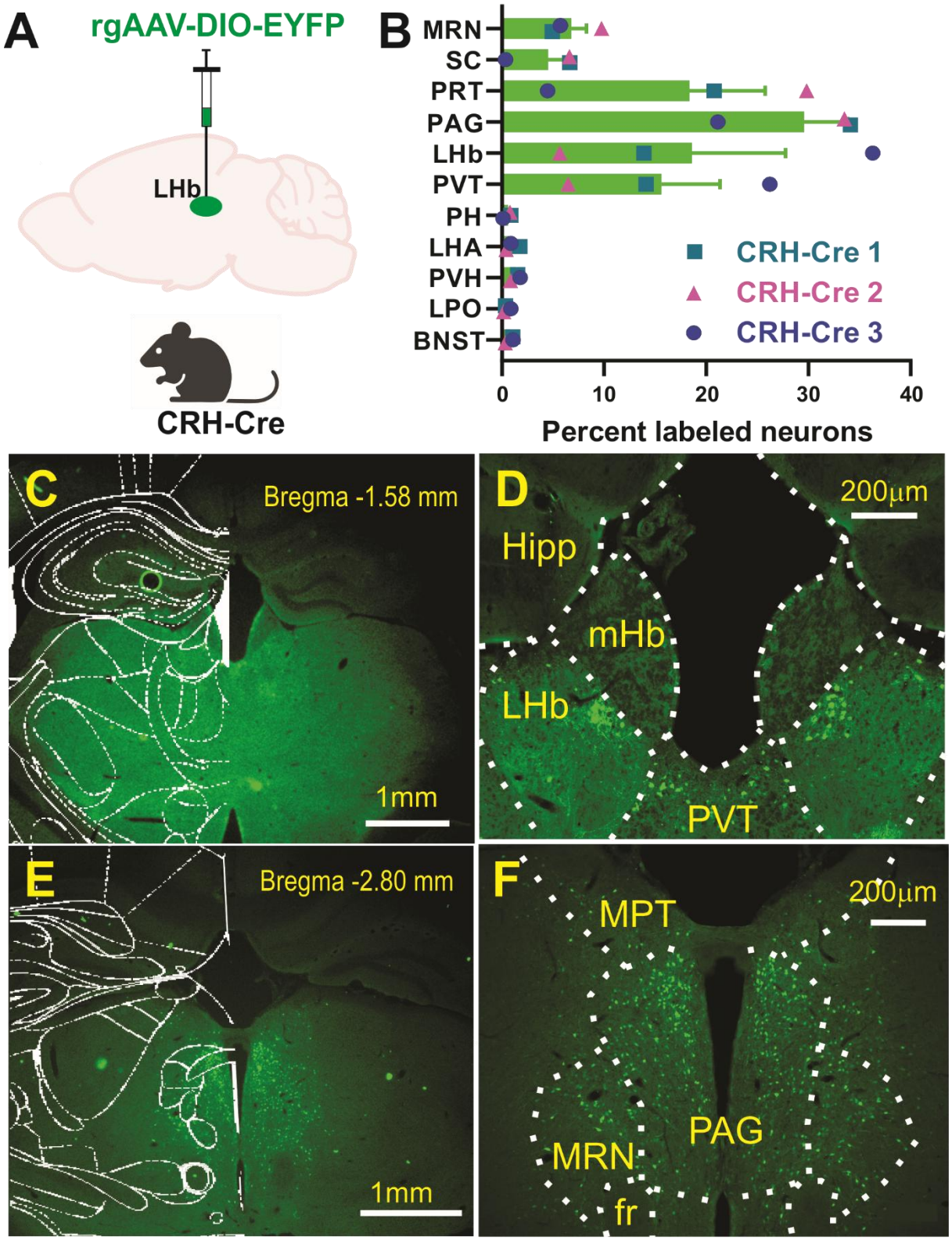

1120

1121 **Figure 1: Retrograde Identification of CRF-Expressing Projections to the Lateral**
1122 **Habenula (LHb)**
1123 **A)** Schematic of the viral strategy using a Cre-dependent retrograde vector (rgAAV-
1124 DIO-EYFP) injected into the LHb of CRH-Cre mice. This approach selectively labels the
1125 cell bodies of CRF-expressing neurons that provide direct input to the LHb. **B)**
1126 Quantitative distribution of retrogradely labeled cell bodies across identified brain
1127 regions. Data are presented as the percentage of total labeled neurons per animal (n=3
1128 mice: 2 males, 1 female). Individual symbols (circles, triangles, squares) represent data
1129 from single subjects (CRH-Cre 1–3); bars indicate the mean. High densities of labeled
1130 cells were observed in the pretectal area (PRT), periaqueductal gray (PAG), LHb, and
1131 paraventricular thalamic nucleus (PVT). Total cells analyzed per subject: CRH-Cre 1
1132 (n=2211), CRH-Cre 2 (n=3309), and CRH-Cre 3 (n=1750). **C, E:** Low-magnification
1133 coronal sections with mouse atlas overlays at the indicated Bregma levels (-1.58 mm
1134 and -2.80 mm), showing the spatial distribution of EYFP+ neurons. **D, F:** High-
1135 magnification images of key regions of interest (ROIs). **D** highlights labeling in the LHb
1136 and PVT; **F** illustrates labeling in the medial pretectal nucleus (MPT, part of the PRT),
1137 PAG, and midbrain reticular nucleus (MRN). Supplementary Figure 1 contains
1138 representative images of the remaining brain regions identified as containing CRF+
1139 neurons projecting to the LHb. Abbreviations: *BNST*, bed nucleus of the stria terminalis;
1140 *LPO*, lateral preoptic area; *LHA*, lateral hypothalamus; *PH*, posterior hypothalamus;
1141 *PVH*, paraventricular hypothalamic nucleus; *SC*, superior colliculus; *fr*, fasciculus
1142 retroflexus. Scale bars: C, E = 1mm; D, F = 200μm.
1143

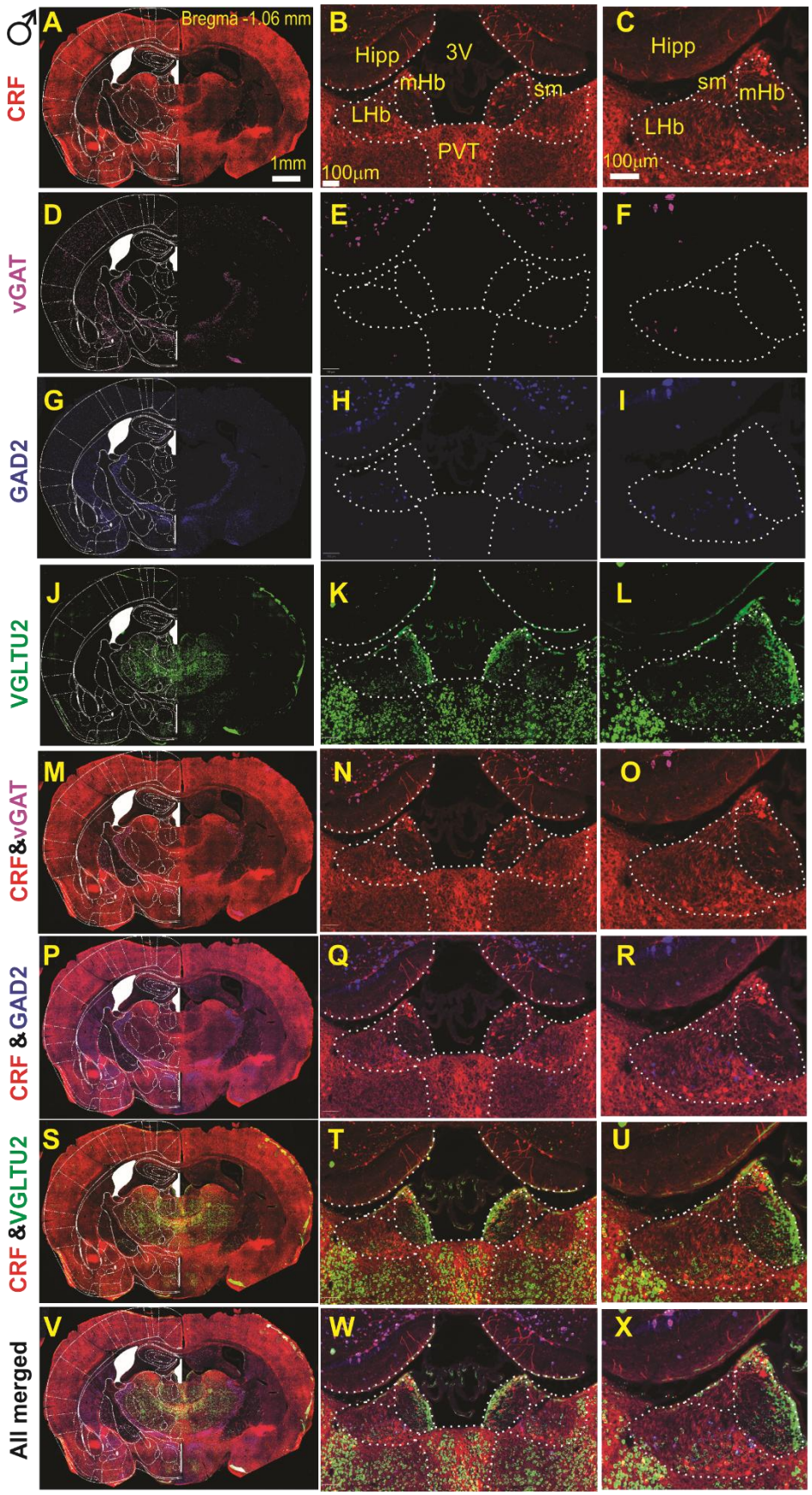
♂
CRF
vGAT
GAD2
VGLTU2
CRF&vGAT
CRF &GAD2
CRF &VGLTU2
All merged
A
Bregma -1.06 mm
1mm
B
Hipp
3V
mHb
sm
LHb
PVT
100µm
C
Hipp
sm
mHb
LHb
100µm
D
E
F
G
H
I
J
K
L
M
N
O
P
Q
R
S
T
U
V
W
X

1144

1145 **Figure 2: Molecular Characterization of CRF+ Neurons in the male LHb at Bregma**
1146 **-1.06mm.**

1147 Multiplexed RNAscope *in situ* hybridization was utilized to identify the neurotransmitter
1148 phenotype of CRF+ (tdTomato-labeled) neurons in male CRH-Cre::Ai14 mice at
1149 Bregma -1.06 mm. (**A**, **D**, **G**, **J**): Low-magnification hemicoronal views integrated with
1150 mouse atlas overlays, showing regional expression patterns of *Crh* (tdTomato), *Slc32a1*
1151 (vGAT), *Gad2* (GAD2), and *Slc17a6* (vGLUT2). (**B**–**L**): High-magnification images
1152 corresponding to panels A, D, G, and J, highlighting bilateral expression within the
1153 lateral habenula (LHb) and providing high-resolution details of the left LHb. (**M**–**U**): Dual-
1154 channel merged images demonstrating the colocalization (overlay) of CRF with
1155 inhibitory markers (*vGAT*, *GAD2*) and the excitatory marker (*vGLUT2*). (**V**–**X**): All-
1156 channel merged images illustrating the simultaneous colocalization of *vGAT*, *GAD2*,
1157 and *vGLUT2* within LHb CRF+ neurons. Abbreviations: *LHb*, lateral habenula; *mHb*,
1158 medial habenula; *Hipp*, hippocampus; *sm*, stria medullaris; *3V*, third ventricle; *PVT*,
1159 paraventricular nucleus of the thalamus. Scale bars: A = 1mm; B, C = 100 μm.
1160

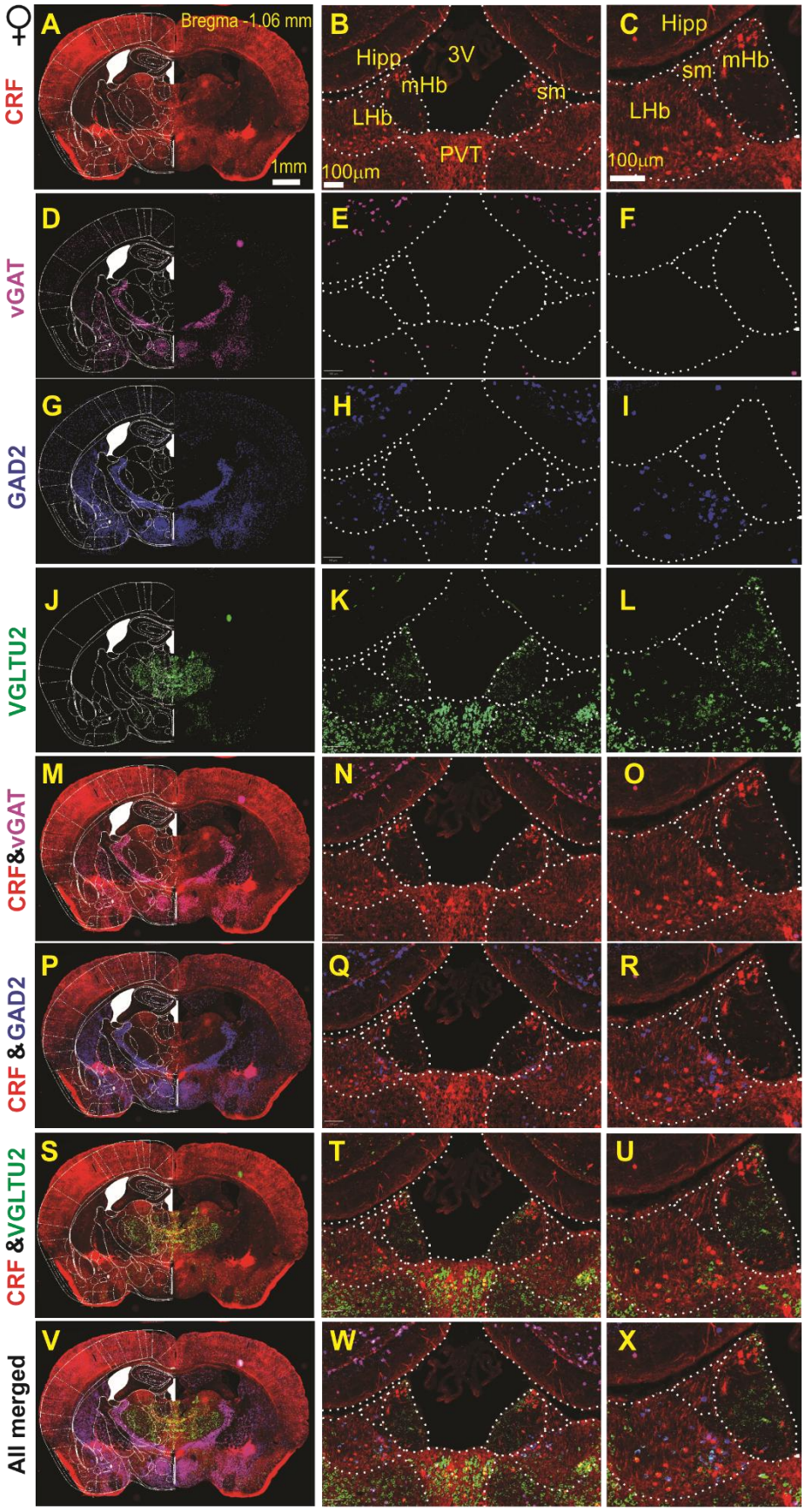
♀
CRF
vGAT
GAD2
VGLTU2
CRF&vGAT
CRF &GAD2
CRF &VGLTU2
All merged
A
Bregma -1.06 mm
1mm
B
Hipp
3V
mHb
sm
LHb
PVT
100μm
C
Hipp
sm
mHb
LHb
100μm
D
E
F
G
H
I
J
K
L
M
N
O
P
Q
R
S
T
U
V
W
X

1161

1162 **Figure 3: Molecular Characterization of CRF+ Neurons in the female LHb at**
1163 **Bregma -1.06mm.**
1164 Multiplexed RNAscope *in situ* hybridization was utilized to identify the neurotransmitter
1165 phenotype of CRF+ (tdTomato-labeled) neurons in female CRH-Cre::Ai14 mice at
1166 Bregma -1.06 mm. (**A**, **D**, **G**, **J**): Low-magnification hemicoronal views integrated with
1167 mouse atlas overlays, showing regional expression patterns of *Crh* (tdTomato), *Slc32a1*
1168 (vGAT), *Gad2* (GAD2), and *Slc17a6* (vGLUT2). (**B**–**L**): High-magnification images
1169 corresponding to panels A, D, G, and J, highlighting bilateral expression within the
1170 lateral habenula (LHb) and providing high-resolution details of the left LHb. (**M**–**U**): Dual-
1171 channel merged images demonstrating the colocalization (overlay) of CRF with
1172 inhibitory markers (*vGAT*, *GAD2*) and the excitatory marker (*vGLUT2*). (**V**–**X**): All-
1173 channel merged images illustrating the simultaneous colocalization of *vGAT*, *GAD2*,
1174 and *vGLUT2* within LHb CRF+ neurons. Abbreviations: *LHb*, lateral habenula; *mHb*,
1175 medial habenula; *Hipp*, hippocampus; *sm*, stria medullaris; *3V*, third ventricle; *PVT*,
1176 paraventricular nucleus of the thalamus. Scale bars: A = 1mm; B, C = 100 μm.
1177
1178
1179
1180
1181
1182
1183

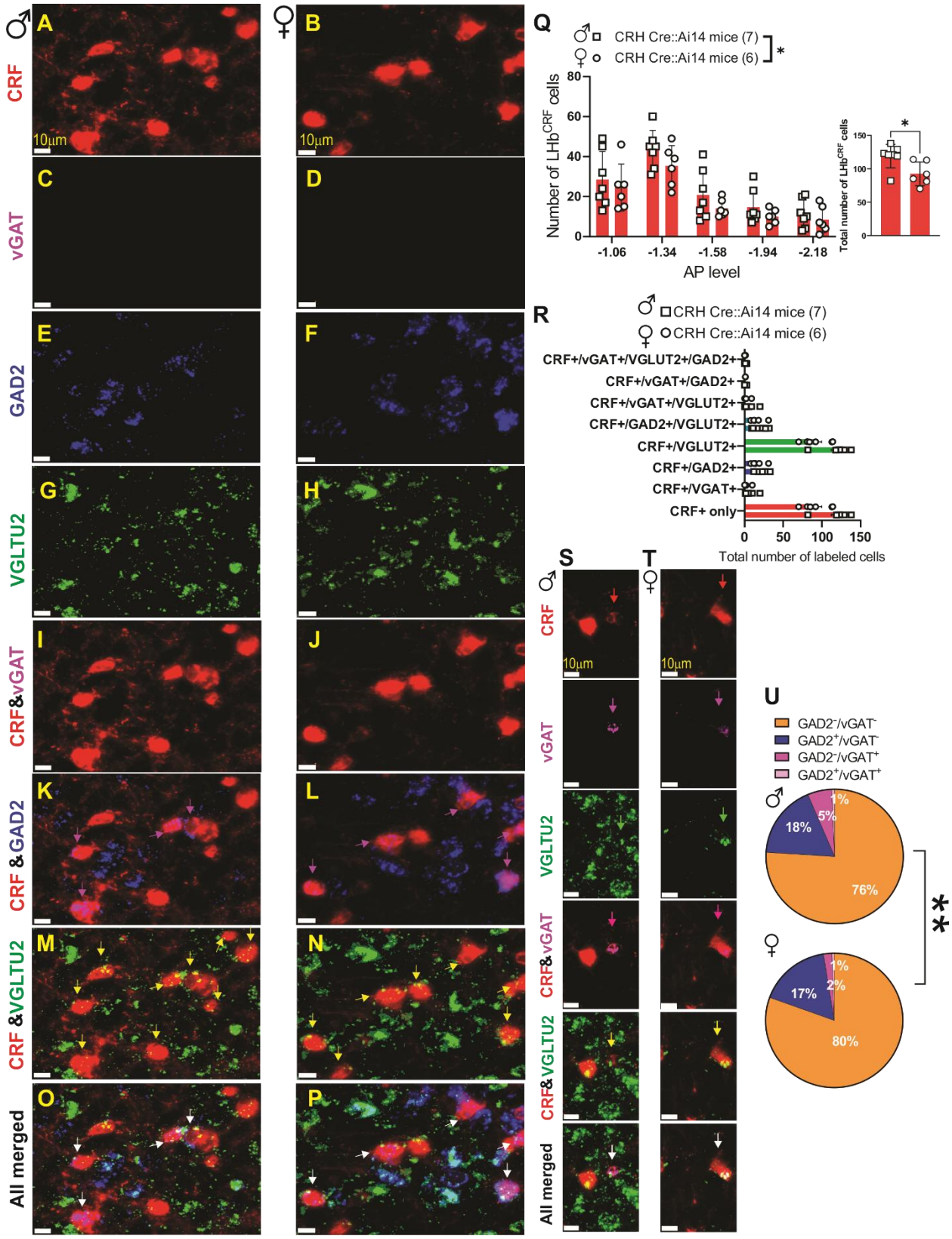
♂
♀
CRF
vGAT
GAD2
VGLTU2
CRF&vGAT
CRF &GAD2
CRF &VGLTU2
All merged
10μm
Q
CRH Cre::Ai14 mice (7)
CRH Cre::Ai14 mice (6)
Number of LHb^CRF cells
AP level
-1.06
-1.34
-1.58
-1.94
-2.18
Total number of LHb^CRF cells
R
CRH Cre::Ai14 mice (7)
CRH Cre::Ai14 mice (6)
CRF+/vGAT+/VGLUT2+/GAD2+
CRF+/vGAT+/GAD2+
CRF+/vGAT+/VGLUT2+
CRF+/GAD2+/VGLUT2+
CRF+/VGLUT2+
CRF+/GAD2+
CRF+/VGAT+
CRF+ only
Total number of labeled cells
S
T
U
GAD2⁻/vGAT⁻
GAD2⁺/vGAT⁻
GAD2⁻/vGAT⁺
GAD2⁺/vGAT⁺
18%
5%
1%
76%
17%
2%
1%
80%

1184

1185 **Figure 4: LHb^{CRF} neurons are predominantly glutamatergic and exhibit sex-**
1186 **dependent distribution.**
1187 **(A–P)** High-resolution representative images from male (left columns) and female (right
1188 columns) mice showing the distribution of *Slc32a1* (vGAT), *Gad2* (GAD2), and *Slc17a6*
1189 (VGLUT2) mRNA. Given the low prevalence of the *vGAT+/CRF+* subpopulation
1190 (quantified in R and U), panels A–P represent the predominant neurochemical
1191 phenotypes: CRF+ neurons expressing vGLUT2 alone, GAD2 alone, or the co-
1192 expression of both markers. **(K, L):** Magenta arrows indicate CRF+ neurons co-
1193 expressing GAD2. **(M, N):** Yellow arrows indicate CRF+ neurons co-expressing
1194 VGLUT2. **(O, P):** White arrows highlight representative neurons showing triple
1195 colocalization of CRF, vGLUT2, and GAD2. **(Q)** Analysis of the number of CRF+
1196 neurons identified per section across five anterior-posterior (AP) levels (-1.06 to -2.18
1197 mm). The inset bar graph represents the total summation of CRF+ neurons across all
1198 analyzed levels. Male mice (squares, n=7) exhibited a significantly higher number of
1199 total LHb CRF+ neurons compared to females (circles, n=6). **(R)** Bar graph illustrating
1200 the frequency of total CRF+ neurons expressing various combinations of GABAergic
1201 and glutamatergic markers. Notably, 100% of identified CRF+ neurons co-express
1202 VGLUT2. While the vast majority are purely glutamatergic, small subpopulations exhibit
1203 dual-phenotypes, co-expressing either GAD2 or vGAT in addition to vGLUT2. No CRF+
1204 neurons were found to be exclusively GABAergic. **(S–T)** High-resolution representative
1205 images from male **(S)** and female **(T)** mice showing the discrete subpopulation of CRF+
1206 neurons co-expressing vGAT and VGLUT2 (indicated by white arrows). **(U)** Pie charts
1207 illustrating the co-expression of GABAergic markers within the total CRF+/vGLUT2+

population. In both sexes, the majority of CRF+ neurons (76–80%) are purely glutamatergic. A consistent proportion (17–18%) also express GAD2. A negligible but statistically distinct subpopulation expresses vGAT in the absence of GAD2 (as shown in S, T). This phenotype exhibited a sex difference, with a higher prevalence in males (5%) compared to females (2%), demonstrating that males possess a significantly larger fraction of CRF glutamatergic neurons carrying the vesicular GABA transporter. Scale bars: 10μm. 2-way ANOVA, Student's t-test Chi-square test; **$p<0.01$.

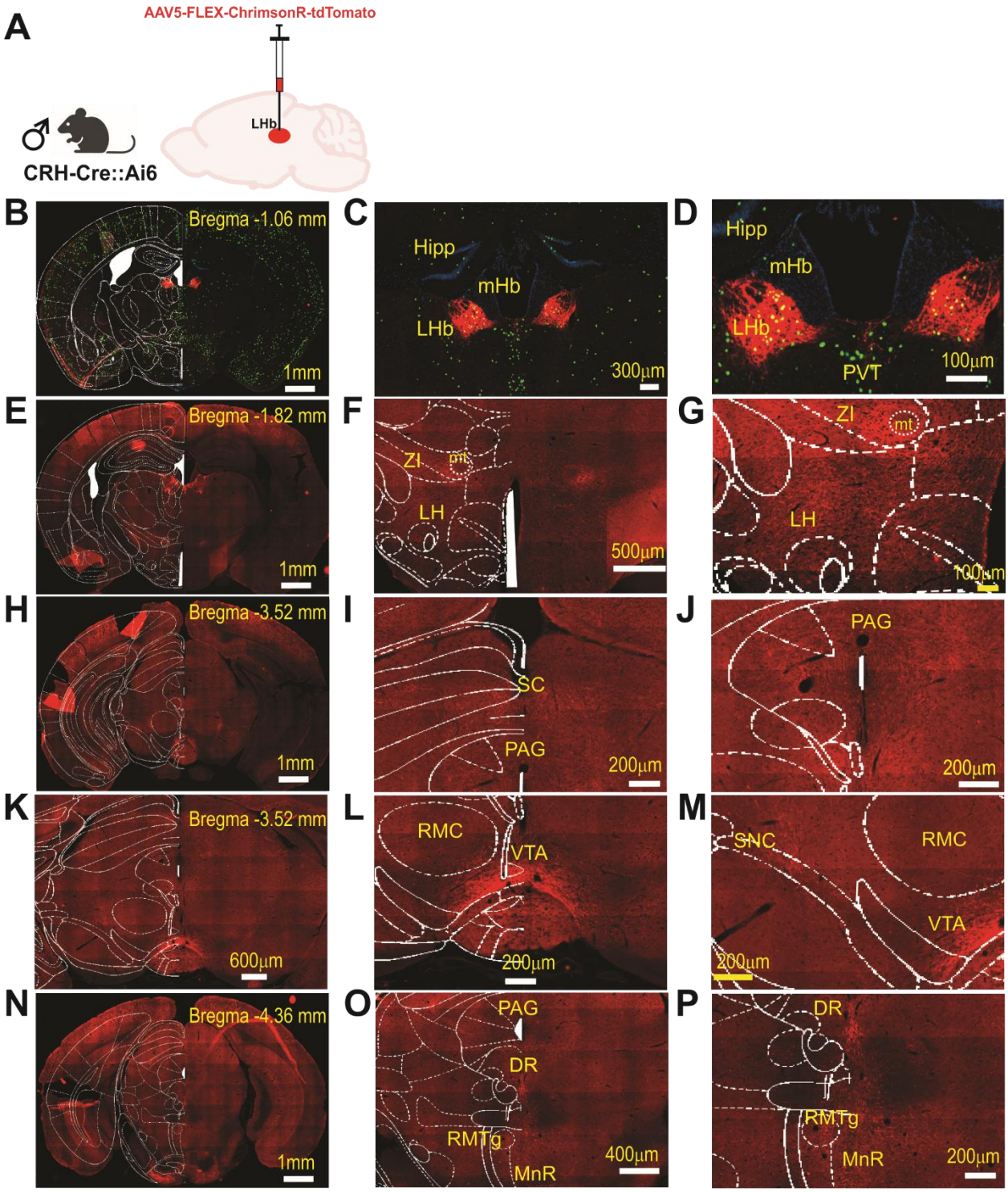

Figure 5: Anterograde Mapping of LHb CRF+ Neuronal Projections in male mice. **(A)** Schematic of the viral approach: a Cre-dependent anterograde vector (AAV5-syn-FLEX-ChrimsonR-tdTomato) was injected into the LHb of male CRH-Cre::Ai6 mice

1220 (n=2). (**B**–**D**) Low-magnification hemicoronal view (**B**) and high-magnification images
1221 (**C**, **D**) of the LHb at Bregma -1.06 mm. Images show the colocalization of endogenous
1222 GFP (from the Ai6 reporter line) and ChrimsonR-tdTomato, confirming the selective
1223 transduction of LHb CRF+ neurons. (**E**–**G**) Representative hemicoronal (E) and high-
1224 magnification (F, G) images illustrating tdTomato-labeled axonal processes originating
1225 from LHb CRF+ neurons within the lateral hypothalamus (LH) and zona incerta (ZI) at
1226 Bregma -1.82mm. (**H**–**J**) Midbrain Projections. Representative hemicoronal (H) and
1227 high-magnification (I, J) images showing dense tdTomato-labeled axonal innervation
1228 within the superior colliculus (**SC**) and periaqueductal gray (**PAG**) at Bregma -3.52mm.
1229 (**K**–**M**) Dopaminergic and Monoaminergic Nuclei. Representative hemicoronal (K) and
1230 high-magnification (L, M) views of labeled LHb CRF+ fibers within the ventral tegmental
1231 area (VTA) and substantia nigra pars compacta (SNc) at Bregma -3.52 mm. (**N**–**P**)
1232 Hindbrain and Raphe Nuclei. Representative hemicoronal (N) and high-magnification
1233 (O, P) images illustrating projection patterns within the periaqueductal gray (PAG),
1234 dorsal raphe (DR), rostromedial tegmental nucleus (RMTg), and median raphe (MnR) at
1235 Bregma -4.36mm. Abbreviations: PVT, paraventricular nucleus of thalamus; RMC, red
1236 nucleus, magnocellular part; mHb, medial habenula; mt, mammillotegmental tract; Hipp,
1237 hippocampus. Scale bars: B, E, H, N = 1mm; K = 600μm; F = 500μm; O = 400μm; C =
1238 300 μm; I, J, L, M, P = 200μm; D, G= 100μm.

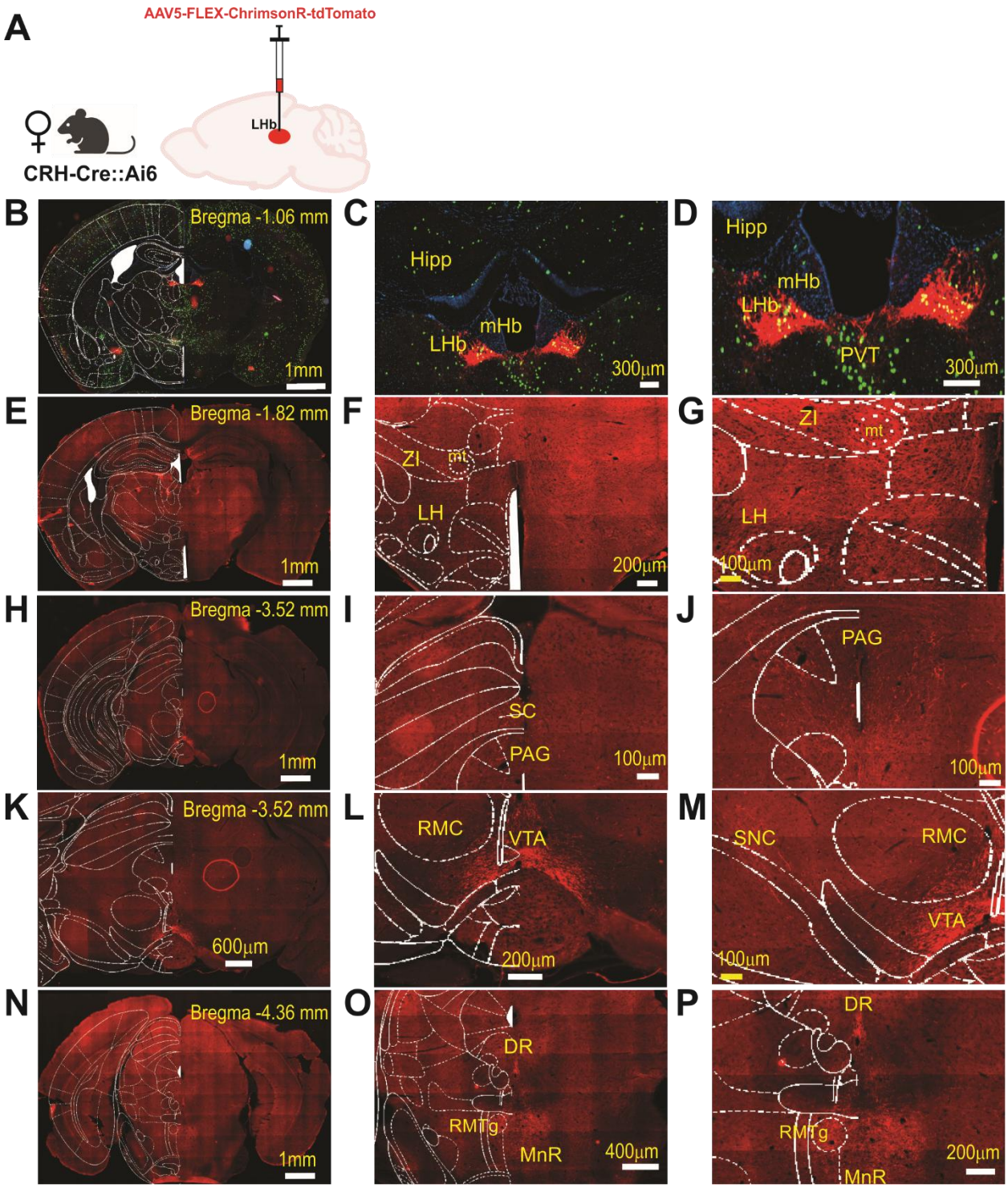

Figure 6: Anterograde Mapping of LHb CRF+ Neuronal Projections in female mice. **(A)** Schematic of the viral approach: a Cre-dependent anterograde vector (AAV5-syn-FLEX-ChrimsonR-tdTomato) was injected into the LHb of female CRH-Cre::Ai6 mice

1243 (n=2). (**B**–**D**) Low-magnification hemicoronal view (**B**) and high-magnification images
1244 (**C**, **D**) of the LHb at Bregma -1.06 mm. Images show the colocalization of endogenous
1245 GFP (from the Ai6 reporter line) and ChrimsonR-tdTomato, confirming the selective
1246 transduction of LHb CRF+ neurons. (**E**–**G**) Representative hemicoronal (E) and high-
1247 magnification (F, G) images illustrating tdTomato-labeled axonal processes originating
1248 from LHb CRF+ neurons within the lateral hypothalamus (LH) and zona incerta (ZI) at
1249 Bregma -1.82mm. (**H**–**J**) Midbrain Projections. Representative hemicoronal (H) and
1250 high-magnification (I, J) images showing dense tdTomato-labeled axonal innervation
1251 within the superior colliculus (**SC**) and periaqueductal gray (**PAG**) at Bregma -3.52mm.
1252 (**K**–**M**) Dopaminergic and Monoaminergic Nuclei. Representative hemicoronal (K) and
1253 high-magnification (L, M) views of labeled LHb CRF+ fibers within the ventral tegmental
1254 area (VTA) and substantia nigra pars compacta (SNc) at Bregma -3.52 mm. (**N**–**P**)
1255 Hindbrain and Raphe Nuclei. Representative hemicoronal (N) and high-magnification
1256 (O, P) images illustrating projection patterns within the periaqueductal gray (PAG),
1257 dorsal raphe (DR), rostromedial tegmental nucleus (RMTg), and median raphe (MnR) at
1258 Bregma -4.36mm. Abbreviations: PVT, paraventricular nucleus of thalamus; RMC, red
1259 nucleus, magnocellular part; mHb, medial habenula; mt, mammillotegmental tract; Hipp,
1260 hippocampus. Scale bars: B, E, H, N = 1mm; K = 600μm; O = 400μm; C, D = 300 μm; F,
1261 L, P = 200μm; G, I, J, M =100μm.
1262
1263
1264
1265

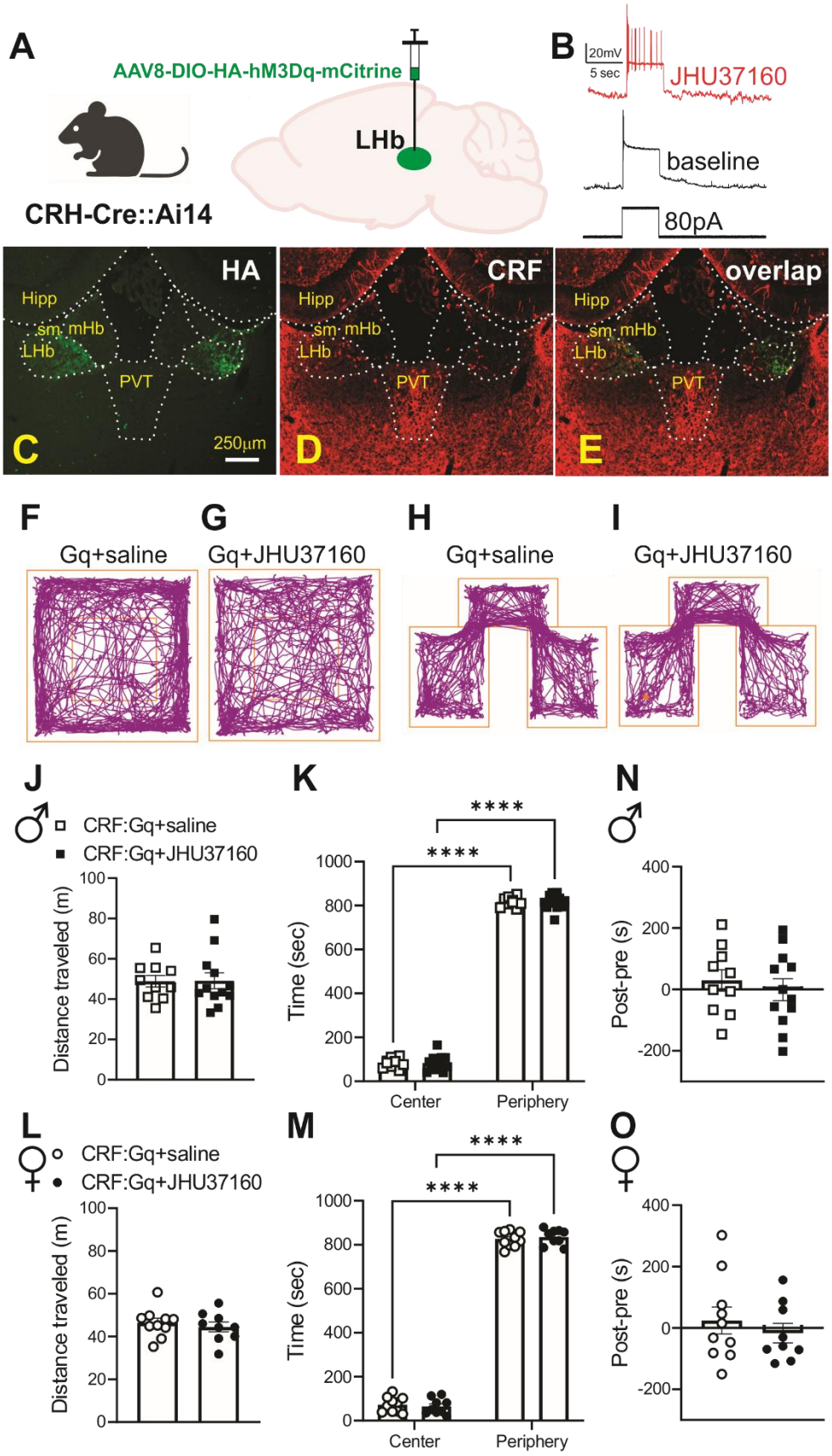
A
AAV8-DIO-HA-hM3Dq-mCitrine
LHb
CRH-Cre::Ai14
B
20mV
5 sec
JHU37160
baseline
80pA
HA
CRF
overlap
Hipp
sm
mHb
LHb
PVT
250µm
C
D
E
F
G
H
I
Gq+saline
Gq+JHU37160
Gq+saline
Gq+JHU37160
J
K
N
CRF:Gq+saline
CRF:Gq+JHU37160
Distance traveled (m)
Time (sec)
Post-pre (s)
****
Center
Periphery
L
M
O
CRF:Gq+saline
CRF:Gq+JHU37160
Distance traveled (m)
Time (sec)
Post-pre (s)
****
Center
Periphery

1266

1267 **Figure 7: Chemogenetic activation of LHb^{CRF} neurons failed to elicit changes in**
1268 **locomotor activity or anxiety-like behavior in the open field test (OFT) and did not**
1269 **induce place preference or aversion in the conditioned place preference Test**
1270 **(CPP). A** Injection schematic: AAV8-DIO-HA-hM3Dq-mCherry into the LHb of a CRH-
1271 Cre::Ai14 mouse. **B** Representative traces of action potential generation in response to
1272 an 80pA current step in an LHb^{CRF} neuron expressing hM3Dq+ before and after bath
1273 application of 100 nM JHU37160. **C-E** Fluorescent images of a coronal LHb section
1274 from a CRH-Cre::Ai14 mouse injected with AAV-DIO-HA-hM3Dq, stained with anti-HA
1275 antibody, confirming co-expression of tdTomato (red) and HA-hM3Dq (green) in LHb^{CRF}
1276 neurons, scale bar 250μm. **F-I** Representative track plots showing mouse movement in
1277 the OFT (**F-G**) and in the saline-/JHU37160-paired and unpaired compartments of the
1278 CPP (**H-I**) for saline- or JHU37160-injected CRH-Cre::Ai14 Gq-DREADD mice. **J-O**
1279 show behavioral data in OFT and CPP in male (squares) and female (circles) mice
1280 treated with either saline (open symbols) or JHU37160 (filled symbols). **J-K** and **L-M**
1281 Quantification of OFT performance revealed no significant differences between
1282 JHU37160- and saline-treated mice of either sex in total distance traveled or time spent
1283 in the center or periphery of the arena. **N-O** CPP analysis showed no evidence of place
1284 preference in JHU37160-paired CRH-Cre::Ai14 Gq-DREADD mice, comparable to
1285 saline-paired ones. Abbreviations: *LHb*, lateral habenula; *mHb*, medial habenula; *Hipp*,
1286 hippocampus; *sm*, stria medullaris; *PVT*, paraventricular nucleus of the thalamus. Scale
1287 bar: C = 250 μm. *****p<0.0001, two-way ANOVA.
1288
1289

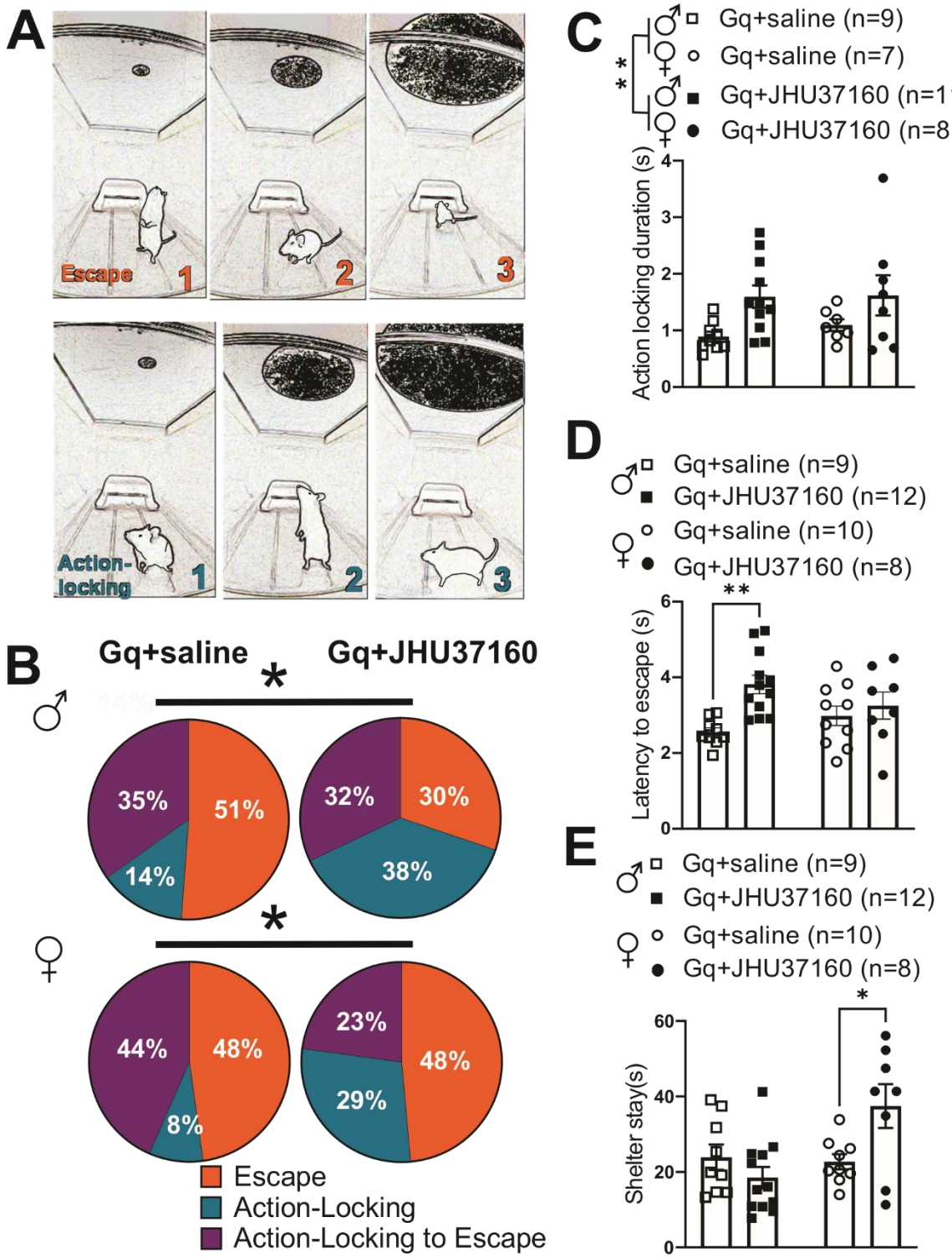

Figure 8: Chemogenetic activation of LHb^{CRF} neurons shifts defensive strategies toward passive action-locking in the Visual Looming Shadow Test (VLST).

1293 **(A)** Representative image sequences illustrating the two primary defensive responses to
1294 a visual looming stimulus: Escape (top row) and action-locking (bottom row).
1295 **(B)** Pie charts illustrating the percentage of trials resulting in action-locking (teal) vs.
1296 escape (orange) as well as action-locking to escape (purple) behaviors in male and
1297 female CRH-Cre::Ai14 mice expressing hM3Dq. In both sexes, administration of the
1298 DREADD agonist JHU37160 significantly increased the prevalence of action-locking
1299 behaviors. **(C–E)** show behavioral parameters in VLST in male (squares) and female
1300 (circles) mice treated with either saline (open symbols) or JHU37160 (filled symbols).
1301 **(C)** Action-locking duration: Activation of LHb^{CRF} neurons resulted in an overall increase
1302 in the duration of action-locking in both male and female mice. Of note, three mice (one
1303 male Gq+JHU, one female Gq+Saline, and one female Gq+JHU) did not exhibit any
1304 action-locking behavior across all trials. **(D)** Latency to escape: Activation of LHb^{CRF}
1305 neurons significantly increased latencies to escape in males. **(E)** Shelter Stay Duration:
1306 Post-escape behavior analysis revealed that chemogenetic activation of LHb^{CRF}
1307 neurons significantly prolonged the duration spent within the shelter specifically in
1308 female mice. Data are presented as mean ±SEM. # $p=0.08$, *$p<0.05$, **$p<0.01$, Chi-
1309 square test, 2-way ANOVA.
1310
1311

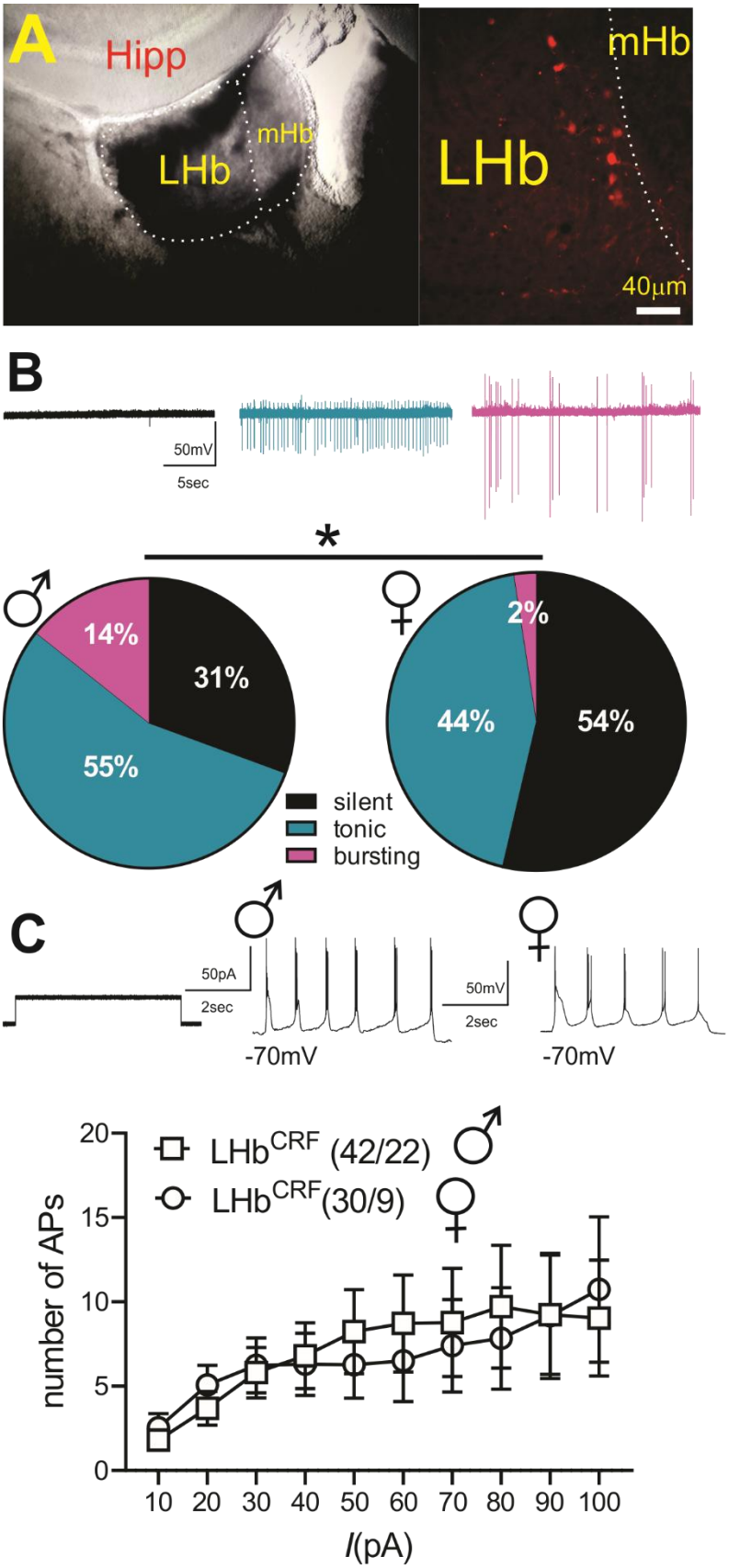
A
Hipp
mHb
LHb
mHb
LHb
40μm
B
50mV
5sec
*
14%
31%
55%
2%
44%
54%
silent
tonic
bursting
C
50pA
2sec
50mV
2sec
-70mV
-70mV
LHbCRF (42/22)
LHbCRF(30/9)
number of APs
0
5
10
15
20
10 20 30 40 50 60 70 80 90 100
I(pA)

1312

1313 **Figure 9: LHb^{CRF} neurons in male CRH-Cre::TdTomato mice exhibit greater**
1314 **spontaneous tonic and bursting activity than in females. A** Coronal habenula slice
1315 images from a CRH-Cre::tdTomato mouse, visualized using IR-DIC (left) and
1316 fluorescence (right; scale bar = 40 μm). **B** Representative traces and pie charts
1317 illustrating spontaneous neuronal activity and the percentage of silent (black), tonic
1318 (blue), or bursting (pink) activity patterns in tdTomato-labeled LHb^{CRF} neurons from
1319 male (n=49 cells/22 mice) and female (n=41 cells/9 mice) CRH-Cre::TdTomato mice
1320 (voltage-clamp, cell-attached recordings at V=0 mV). **C** Action potential (AP) generation
1321 in response to depolarizing current steps in tdTomato-labeled LHb^{CRF} neurons, recorded
1322 under conditions of intact synaptic transmission, with representative traces from male
1323 (black open squares, n=42 cells/22 mice) and female (black open circles, 30 cells/9
1324 mice) CRH-Cre::TdTomato mice. *$p<0.05$; Chi-square test. Scale bars: A = 40 μm.
1325

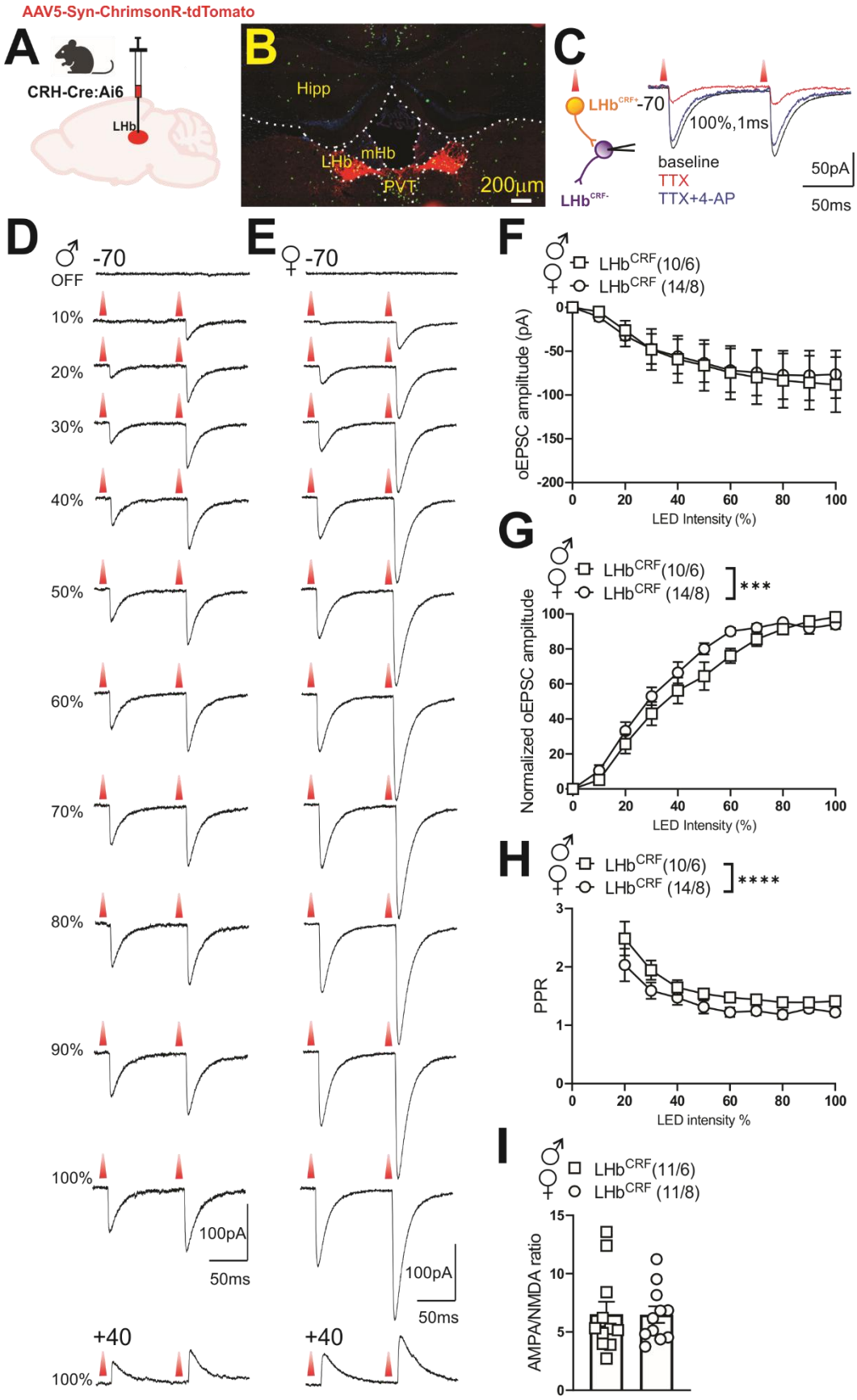
AAV5-Syn-ChrimsonR-tdTomato
A
CRH-Cre:Ai6
LHb
B
Hipp
LHb
mHb
PVT
200µm
C
LHb^CRF+
-70
100%,1ms
baseline
TTX
TTX+4-AP
50pA
50ms
LHb^CRF-
D
♂ -70
OFF
10%
20%
30%
40%
50%
60%
70%
80%
90%
100%
100pA
50ms
+40
100%
E
♀ -70
100pA
50ms
+40
F
♂
♀
LHb^CRF(10/6)
LHb^CRF (14/8)
oEPSC amplitude (pA)
LED Intensity (%)
G
LHb^CRF(10/6)
LHb^CRF (14/8)
***
Normalized oEPSC amplitude
LED Intensity (%)
H
LHb^CRF(10/6)
LHb^CRF (14/8)
****
PPR
LED intensity %
I
LHb^CRF(11/6)
LHb^CRF (11/8)
AMPA/NMDA ratio

1326

1327 **Figure 10: LHb CRF+ Neurons form local monosynaptic glutamatergic**
1328 **connections with non-CRF neurons.**
1329 **(A)** Schematic illustrating the injection of a Cre-dependent anterograde vector (AAV5-
1330 Syn-FLEX-ChrimsonR-tdTomato) into the LHb of CRH-Cre::Ai6 mice to dissect local
1331 synaptic connectivity. **(B)** High-magnification image demonstrating the restricted
1332 expression of ChrimsonR-tdTomato within LHb CRF+ neurons and their local terminal
1333 fields. **(C)** Schematic and representative traces of optically evoked excitatory
1334 postsynaptic currents (oEPSCs) recorded from a non-CRF (GFP-negative) LHb neuron.
1335 Inward currents recorded at -70mV (black trace) were almost completely abolished by
1336 the sodium channel blocker TTX (1μM; red trace) and subsequently rescued by the
1337 addition of the potassium channel blocker 4-AP (50μM; blue trace), confirming the
1338 monosynaptic nature of the connection. **(D, E)** Representative traces of paired-pulse
1339 oEPSCs recorded at -70mV from male (D) and female (E) mice across increasing LED
1340 intensities (10–100%). Bottom traces illustrate mixed AMPA- and NMDA-mediated
1341 oEPSCs recorded at +40mV at maximal (100%) LED intensity. **(F)** Mean oEPSC
1342 amplitudes (measured from the first pulse) across increasing LED intensities for male
1343 (squares) and female (circles) mice. **(G)** Normalized oEPSC amplitudes expressed as a
1344 percentage of the minimum and maximum response per cell to account for variability in
1345 viral expression. **(H)** Paired-Pulse Ratio (PPR). Quantification of the PPR (P2/P1)
1346 across LED intensities male (squares) and female (circles) mice. **(I)** AMPA/NMDA
1347 Ratios. Mean AMPA/NMDA ratios recorded from LHb CRF^{-} neurons in male (squares)
1348 and female (circles) mice, showing no significant sex differences in postsynaptic
1349 receptor composition. In all graphs, n =cells/mice. Data are presented as mean±SEM.

1350 Abbreviations: *Hipp*, hippocampus; *mHb*, medial habenula; *PVT*, paraventricular
1351 nucleus of the thalamus. Scale bars: B = 200μm. ***p<0.001, ****p<0.0001; Student's t-
1352 test and 2-way ANOVA.
1353
1354
1355
1356
1357
1358
1359
1360
1361
1362
1363